The Astrophysical Journal, 935:114 (17pp), 2022 August 20 https://doi.org/10.3847/1538-4357/ac80be

Compton-thick AGN in the NuSTAR Era. VIII. A joint NuSTAR–XMM-Newton Monitoring of the Changing-look Compton-thick AGN NGC 1358

S. Marchesi[1,2], X. Zhao[2,3], N. Torres-Albà[2], M. Ajello[2], M. Gaspari[4], A. Pizzetti[2], J. Buchner[5], E. Bertola[1,6], A. Comastri[1], A. Feltre[1], R. Gilli[1], G. Lanzuisi[1], G. Matzeu[6], F. Pozzi[1,6], F. Salvestrini[7], D. Sengupta[1,6], R. Silver[2], F. Tombesi[8,9,10,11,12], A. Traina[1,6], C. Vignali[1,6], and L. Zappacosta[9]
[1] INAF—Osservatorio di Astrofisica e Scienza dello Spazio di Bologna, Via Piero Gobetti, 93/3, I-40129, Bologna, Italy; stefano.marchesi@inaf.it
[2] Department of Physics and Astronomy, Clemson University, Kinard Lab of Physics, Clemson, SC 29634, USA
[3] Center for Astrophysics | Harvard & Smithsonian, 60 Garden Street, Cambridge, MA 02138, USA
[4] Department of Astrophysical Sciences, Princeton University, Princeton, NJ 08544, USA
[5] Max Planck Institute for Extraterrestrial Physics, Giessenbachstrasse, D-85741 Garching, Germany
[6] Dipartimento di Fisica e Astronomia "Augusto Righi", Università di Bologna, via Gobetti 93/2, I-40129 Bologna, Italy
[7] INAF—Osservatorio Astrofisico di Arcetri, Largo E. Fermi 5, I-50125, Firenze, Italy
[8] Department of Physics, Tor Vergata University of Rome, Via della Ricerca Scientifica 1, I-00133 Rome, Italy
[9] INAF—Osservatorio Astronomico di Roma, Via Frascati 33, I-00078 Monte Porzio Catone, Italy
[10] Department of Astronomy, University of Maryland, College Park, MD 20742, USA
[11] NASA Goddard Space Flight Center, Greenbelt, MD 20771, USA
[12] INFN—Roma Tor Vergata, Via della Ricerca Scientifica 1, I-00133 Rome, Italy
Received 2022 April 23; revised 2022 June 30; accepted 2022 July 11; published 2022 August 22

Abstract

We present the multi-epoch monitoring with NuSTAR and XMM-Newton of NGC 1358, a nearby Seyfert 2 galaxy whose properties made it a promising candidate X-ray changing-look active galactic nucleus (AGN), i.e., a source whose column density could transition from its 2017 Compton-thick (having LOS hydrogen column density $N_{\rm H,LOS} > 10^{24}$ cm^{-2}) state to a Compton-thin ($N_{\rm H,LOS} < 10^{24}$ cm^{-2}) one. The multi-epoch X-ray monitoring confirmed the presence of significant $N_{\rm H,LOS}$ variability over timescales of weeks to years, and allowed us to confirm the *changing-look* nature of NGC 1358, which has most recently been observed in a Compton-thin status. Multi-epoch monitoring with NuSTAR and XMM-Newton is demonstrated to be highly effective in simultaneously constraining three otherwise highly degenerate parameters: the torus average column density and covering factor, and the inclination angle between the torus axis and the observer. We find a tentative anticorrelation between column density and luminosity, which can be understood under the framework of chaotic cold accretion clouds driving recursive AGN feedback. The monitoring campaign of NGC 1358 has proven the efficiency of our newly developed method to select candidate $N_{\rm H,LOS}$-variable, heavily obscured AGN, which we plan to soon extend to a larger sample to better characterize the properties of the obscuring material surrounding accreting supermassive black holes, as well as to constrain AGN feeding models.

Unified Astronomy Thesaurus concepts: Astrophysical black holes (98); Active galactic nuclei (16); X-ray active galactic nuclei (2035); Accretion (14)

1. Introduction

Obscuration in active galactic nuclei (AGNs) has been largely studied over the electromagnetic spectrum, from the optical (e.g., Lawrence 1991; Simpson 2005), to the infrared (e.g., Jaffe et al. 2004; Nenkova et al. 2008a; Feltre et al. 2012), and to X-rays (Gilli et al. 2007; Ricci et al. 2015; Hickox & Alexander 2018). It is commonly accepted that the obscuration is mostly caused by a *dusty torus*, i.e., a distribution of molecular gas and dust located at ∼1–10 pc from the accreting supermassive black hole (SMBH). While the existence of this obscuring material is universally accepted, its geometrical distribution and chemical composition are still a matter of debate. Several works have reported observational evidence favoring a *clumpy torus* scenario, where the obscuring material is distributed in clumps formed by optically thick clouds (e.g., Jaffe et al. 2004; Elitzur & Shlosman 2006; Hönig & Beckert 2007; Risaliti et al. 2007; Nenkova et al. 2008a; Burtscher et al. 2013). Theoretical/numerical models of accretion onto SMBHs also predict a highly clumpy and chaotic multiphase medium (Gaspari et al. 2013, 2017, 2020 for a review), in particular within $r < 100$ pc of the AGN, where chaotic cold accretion (CCA) is expected to boost the feeding rates. Such CCA *rain* has been now observationally probed in many systems and bands spanning from X-ray to optical/IR and radio (e.g., Gaspari et al. 2019; Rose et al. 2019; Maccagni et al. 2021; McKinley et al. 2022; Olivares et al. 2022; Temi et al. 2022).

If the obscuring environment is indeed inhomogeneous, one would expect to observe significant variability in the obscuring material line-of-sight (LOS) column density ($N_{\rm H,LOS}$), and even, in some cases, a transition from a Compton-thick scenario (where $N_{\rm H,LOS} > 10^{24}$ cm^{-2}) to a Compton-thin one (where $N_{\rm H,LOS} < 10^{24}$ cm^{-2}). This transition should occur in a period of time as short as a day and as long as several months, assuming a typical range of obscuring clouds filling factors, velocities, and distances from the accreting BH (e.g., Nenkova et al. 2008a). However, the number of bona fide Compton-thick (CT)-AGN with high-quality X-ray data is limited (∼35 sources, see, e.g., Arévalo et al. 2014; Baloković et al. 2014;

Koss et al. 2015; Masini et al. 2016; Oda et al. 2017; Marchesi et al. 2018, 2019; Torres-Albà et al. 2021; Traina et al. 2021; Zhao et al. 2021), and only a small fraction of these objects have multi-epoch observations on timescales that vary from weeks to years, which are key to properly assess any variation in $N_{\rm H,LOS}$ and/or flux. Consequently, only a few sources have been observed to transition from Compton thick to Compton thin: NGC 1365 (Risaliti et al. 2005); NGC 7582 (Bianchi et al. 2009; Rivers et al. 2015); Mrk 3 (Guainazzi et al. 2012); NGC 454 (Marchese et al. 2012); ESO 323-G77 (Miniutti et al. 2014); and IC 751 (Ricci et al. 2016).

This class of *X-ray changing-look sources* is the ideal $N_{\rm H,LOS}$-variable sample to study the properties of the obscuring material in a complete, self-consistent way. In fact, Compton-thick to Compton-thick $N_{\rm H,LOS}$ transitions are difficult to reliably measure with small enough uncertainties to enable the estimate of the SMBH-cloud distance from $\Delta N_{\rm H,LOS}$, since at column densities above $\sim$2–3 $\times$ 10^{24} cm^{-2} almost all photons at energies <10–20 keV are absorbed by the obscuring material (see, e.g., Koss et al. 2016). In less obscured AGN ($N_{\rm H,LOS} \lesssim 10^{23}$ cm^{-2}), instead, the $N_{\rm H,LOS}$ variability can be measured with excellent precision. However, in this class of objects the overall X-ray emission is dominated by the transmitted main component: consequently, it is difficult to accurately measure the obscuring material properties linked to the reprocessed emission, such as the covering factor and the average column density. Consequently, the limited sample size of currently available X-ray changing-look AGNs prevents us from getting a complete picture of the properties of the obscuring material surrounding accreting SMBHs.

In this paper, we present the result of multi-epoch monitoring of the nearby CT-AGN NGC 1358, a Seyfert 2 galaxy whose properties make it a promising changing-look candidate and an ideal pilot source to start the X-ray characterization of the obscuring material in nearby accreting SMBHs. The work is organized as follows: in Section 2, we present the source, with a particular focus on previous X-ray works. In Section 3, we present the data analysis and results of the joint spectral fitting for the new and old NuSTAR and XMM-Newton observations. We then discuss in Section 4 how the results of the X-ray monitoring can be explained in the framework of a *clumpy obscuration* model. Finally, we summarize the results of our work in Section 5.

Throughout the rest of the work, we assume a flat Λ cold dark matter cosmology with $H_0 = 69.6$ km s^{-1} Mpc^{-1}, $\Omega_m = 0.29$, and $\Omega_\Lambda = 0.71$ (Bennett et al. 2014). Errors are quoted at the 90% confidence level, unless otherwise stated.

2. NGC 1358

NGC 1358 is a nearby ($z = 0.01344$ Theureau et al. 1998), X-ray bright (having 15–150 keV observed flux $f_{15-150\,\rm keV} \geqslant 5 \times 10^{-12}$ erg s^{-1} cm^{-2}) Seyfert 2 galaxy. The source was originally classified as a narrow-line Seyfert 2 source in Filippenko & Sargent (1985) using the Double Spectrograph mounted on the Palomar 200 inch Hale Telescope. A new optical spectrum of NGC 1358 was then taken in 2004 within the 6dF Galaxy Survey, using the multi-object spectrograph mounted on the 1.2 m UK Schmidt Telescope (Jones et al. 2009), and no evidence for optical variability with respect to the Filippenko & Sargent (1985) spectrum is observed, thus confirming the narrow-line nature of the source. We report both optical spectra in Figure 1. More recently, Mason et al. (2015) reported that the near-IR (NIR) spectrum of NGC 1358, obtained using the GNIRS spectrograph mounted on the Gemini North 8 m telescope "only contain[ed] a handful of weak emission lines" (see Figure 1, bottom panel). No evidence for a significant optical changing-look behavior has therefore ever been observed in NGC 1358.

In the X-rays, NGC 1358 is detected in the Swift (Gehrels et al. 2004) Burst Alert Telescope (BAT; Barthelmy et al. 2005) 150 month catalog (K. Iman et al. 2022, in preparation[13]) and has been targeted several times by X-ray telescopes.[14] The first 10 ks XMM-Newton observation was taken in 2005 and analyzed in Marinucci et al. (2012). They determined that NGC 1358 is heavily obscured, and potentially a CT-AGN, but the low data quality made their LOS column density poorly constrained ($N_{\rm H,LOS} = 1.3^{+8.5}_{-0.6} \times 10^{24}$ cm^{-2}). A second observation was performed by Chandra in 2015 November: the joint fit of the Chandra spectrum with the Swift-BAT 100 month one is reported in Marchesi et al. (2017). The source was once again found to be heavily obscured, having $N_{\rm H,LOS} = 1.0^{+0.4}_{-0.6} \times 10^{24}$ cm^{-2}. However, while a physically self-consistent spectral model such as `MYTorus` (Murphy & Yaqoob 2009) was used to perform the fit, the limited count statistic (<100 net counts in the 0.5–7 keV band) of the Chandra spectrum did not allow for a reliable characterization of the obscuring material's physical and geometrical properties.

For this reason, NGC 1358 was subsequently targeted by a joint NuSTAR and XMM-Newton observation performed in 2017 August, whose results are reported in Zhao et al. (2019). The high count statistic in the 0.5–70 keV band obtained in this deep observation (>4500 net counts, $\sim$50% of which detected by NuSTAR in the 3–50 keV band) made it possible to use models that self-consistently characterize AGN obscuration in X-ray spectra, such as `MYTorus` (Murphy & Yaqoob 2009; Yaqoob 2012; Yaqoob et al. 2015) and `borus02` (Baloković et al. 2018). In particular, `borus02` measures important physical and geometric parameters such as the obscuring material LOS column density, its average column density (see Section 3.2.1 for more details on this quantity), and its covering factor, among others. NGC 1358 was found to have (i) LOS column density, $N_{\rm H,LOS} = 2.4^{+0.4}_{-0.1} \times 10^{24}$ cm^{-2}, well above the Compton-thick threshold, at a $>3\,\sigma$ confidence level; (ii) Compton-thin average column density, $N_{\rm H,tor} = 6.5^{+0.5}_{-1.6} \times 10^{23}$ cm^{-2}, i.e., $\sim$4 times smaller than the LOS column density; (iii) low-covering factor ($f_c < 0.15$). The large $\Delta N_{\rm H}$ ($\log(N_{\rm H,LOS})$–$\log(N_{\rm H,tor}) \sim 0.6$) measured in NGC 1358, combined with its low f_c suggests that this source is a promising candidate *clumpy torus* CT-AGN, where the obscuring material is distributed in clumps at the micro to mesoscale (i.e., within a few parsecs from the SMBH, Gaspari et al. 2020), rather than uniformly. Notably, the large $\Delta N_{\rm H}$ measured using `borus02` was independently confirmed using `MYTorus` in its *decoupled* configuration (Yaqoob 2012; Yaqoob et al. 2015), which allows one to independently measure $N_{\rm H,LOS}$ and $N_{\rm H,tor}$.

Based on the abovementioned observational evidence, NGC 1358 is likely to have been observed through an overdense region embedded in a significantly less dense environment. In

[13] An online version of the catalog is available at https://science.clemson.edu/ctagn/bat-150-month-catalog/.

[14] While NGC 1358 has been observed multiple times by Swift-XRT, none of the observations had enough counts to perform a spectral fit. We therefore do not include the Swift-XRT observations in this work.

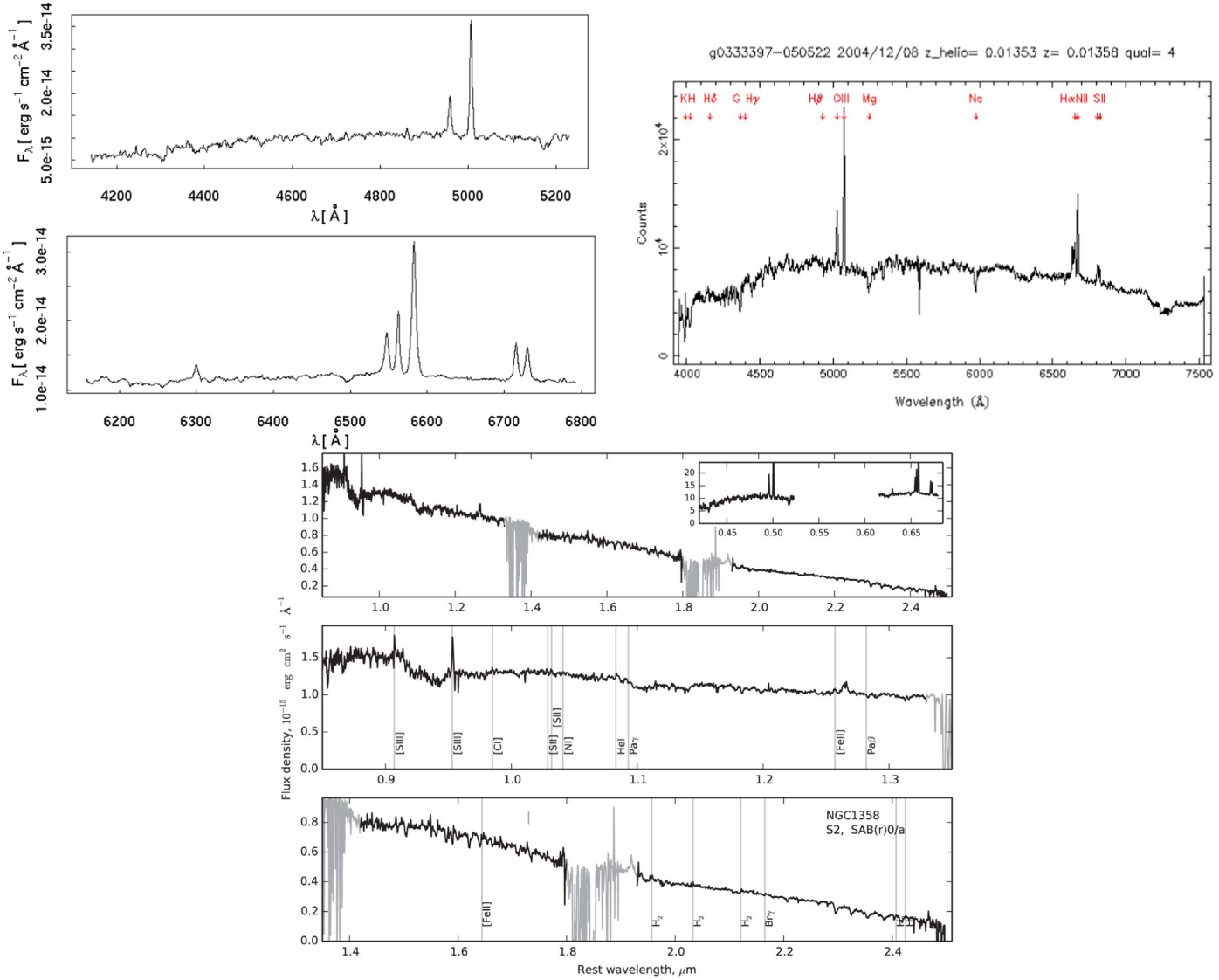

Figure 1. Top panels: optical spectra of NGC 1358 obtained using the Double Spectrograph mounted on the Palomar 200 inch Hale Telescope (Filippenko & Sargent 1985, left; spectrum taken in 1985) and using the multi-object spectrograph mounted on the 1.2 m UK Schmidt Telescope (Jones et al. 2009, right; spectrum taken in 2004). Bottom panel: NIR spectrum of NGC 1358 obtained using the Gemini Near-IR Spectrograph on the Gemini North telescope (Mason et al. 2015, spectrum taken in 2011).

such a scenario, the small covering factor measured with `borus02` would imply that the overall cloud volume filling factor is small, and the obscuring clouds occupy only a fractional part of the parsec-scale region that surrounds the accreting SMBH where the obscuration is expected to take place. Sources with this type of *low-covering factor* obscurer are ideal candidate X-ray changing-look AGN. In objects with large f_c, instead, the number of clouds between the observer and the SMBH is expected to always be $\gg$1, thus significantly reducing the chance of observing a significant change in $N_{\rm H,LOS}$. Notably, at least two CT-AGN fulfill the proposed selection criteria and are known to be variable. NGC 4945 has been shown to vary significantly even above 10 keV, likely because of a combination of intrinsic luminosity and LOS column density variability (Puccetti et al. 2014), while the LOS column density of the material surrounding MRK 3 has been measured at both Compton-thick and Compton-thin levels in the past years (see, e.g., Guainazzi et al. 2012; Yaqoob et al. 2015). We highlight both these sources in Figure 2.

To confirm the clumpy nature of its circumnuclear material, NGC 1358 has been selected for a long-term monitoring campaign with NuSTAR and XMM-Newton, aimed at detecting significant flux and $N_{\rm H,LOS}$ variability. A joint NuSTAR–XMM-Newton monitoring campaign is the best (if not the only) possible approach to constrain the properties of the obscuring material surrounding accreting SMBHs. XMM-Newton alone would not be able to detect potential variability above 10 keV, which can be linked to a variation in the covering factor (see, e.g., Puccetti et al. 2014; Zaino et al. 2020, on the variability above 10 keV observed in the nearby Compton-thick sources NGC 4945 and NGC 1068, respectively). Furthermore, high-quality data at $E > 10$ keV are key to breaking the $N_{\rm H,LOS}$-photon index degeneracy in heavily obscured sources (see, e.g., Marchesi et al. 2019). NuSTAR, however, has a $\sim$4 times lower energy resolution than XMM-Newton at 6.4 keV, around the Fe K line region, and does not cover the energy range $<$3 keV, which is required to tightly

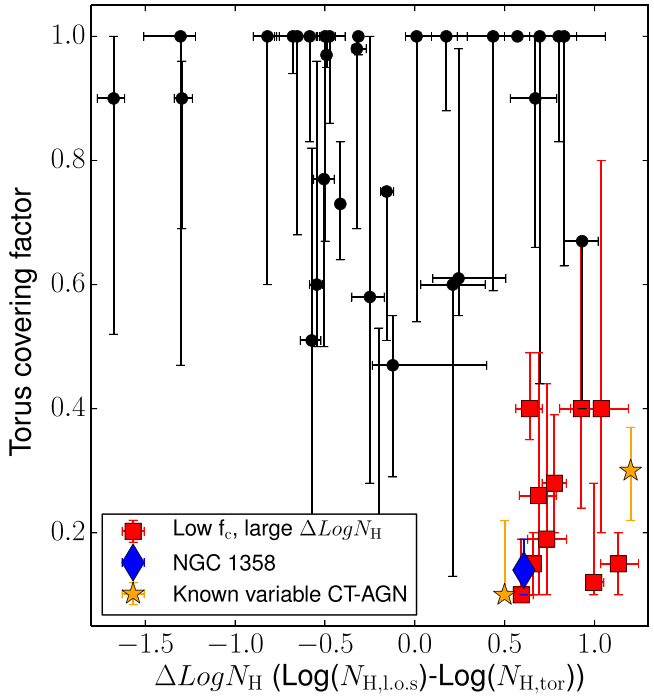

Figure 2. Obscuring material covering factor (f_c) as a function of the difference (ΔLog$N_{\rm H}$) between the logarithms of the LOS and torus average column density, for a sample of nearby CT-AGNs observed with NuSTAR and a 0.5–10 keV facility (XMM-Newton, Chandra, or Swift-XRT; from Marchesi et al. 2019; Torres-Albà et al. 2021). Sources with $f_c < 0.4$ and ΔLog$N_{\rm H} > 0.5$ are plotted as red squares. NGC 1358 is shown as a blue diamond: its large $\Delta N_{\rm H}$ and low f_c make it an excellent candidate clumpy environment CT-AGN. MRK 3 and NGC 4945, both known variable CT-AGN also having large $\Delta N_{\rm H}$ and low f_c, are plotted as orange stars.

constrain $N_{\rm H,LOS}$, and consequently, the AGN intrinsic luminosity.

Among the promising changing-look candidates with low f_c and large $\Delta N_{\rm H}$ reported in (Marchesi et al. 2019, see also the red points in Figure 2), the tentative evidence for LOS column density variability between the 2015 and 2017 observations further strengthens a clumpy obscuration scenario for NGC 1358. This makes it an ideal pilot source to start the X-ray characterization of a whole class of clumpy obscuration CT-AGNs.

3. Data Analysis and Spectral Fitting Results

In this work, we analyze four XMM-Newton and three NuSTAR observations that were taken between 2021 February and 2022 February. The first XMM-Newton observation (nominal length: 36 ks) was taken as part of the XMM-Newton proposal 086298 (PI: S. Marchesi), while the remaining three XMM-Newton observations (nominal length: 30 ks) and the NuSTAR ones (30 ks) are part of a NuSTAR observing program (proposal ID: 07192; PI: S. Marchesi). We report a summary of these observations in Table 1. In the rest of the paper, all the quoted errors are computed at the 90% confidence level for a single parameter of interest.

3.1. Data Reduction

The NuSTAR data are obtained from both focal plane modules, FPMA and FPMB. We calibrated, cleaned, and screened the raw files using the NuSTAR `nupipeline` script version 2.1.1. The NuSTAR calibration database (CALDB) used in this work is version 20210210. We then generated the ARF, RMF, and light-curve files with the `nuproducts` script. Both source and background spectra were extracted from a 60″ radius circle: this choice of radius was found to maximize the signal-to-noise ratio in the source spectra. The background spectra are extracted from a region nearby the source that is not affected by emission from NGC 1358 or other bright objects. Finally, the spectra are binned with a minimum of 15 counts per bin using the `grppha` task.

The XMM-Newton observations taken in 2021 August and 2022 January were performed quasi-simultaneously to the NuSTAR ones, the start and end times of each pair of observations being always less than 12 hr apart (see Table 1). The 2022 February one has instead been taken ∼1 day after the NuSTAR one, thus allowing us to perform a further variability study (as discussed in Section A4). We reduced the XMM-Newton data using the Science Analysis System (Jansen et al. 2001) version 19.1. The 2021 August and 2022 February observations were affected by strong flares, so the net exposure time is 10%–20% (30%–50%) shorter than the nominal one for the MOS (pn) cameras. The MOS (pn) source spectra were extracted from a 10″ (15″) radius circle, while the background spectra are extracted from a 45″ radius circle located nearby NGC 1358 and in a region with no significant contamination from other sources.

Table 1
Summary of the NuSTAR and/or XMM-Newton Observations of NGC 1358 Used in This Work

Instrument	Sequence ObsID	Start Time (UTC)	End Time (UTC)	Exposure (ks)	Net Count Rate (10^{-2} counts s^{-1})
XMM-Newton	0795680101	2017-8-1T17:05:27	2017-8-2T06:03:10	48; 48; 48	0.98 ± 0.05; 0.91 ± 0.05; 3.68 ± 0.15
NuSTAR	60301026002	2017-8-1T03:41:09	2017-8-2T06:36:09	50	2.32 ± 0.07; 2.28 ± 0.07
XMM-Newton	0862980101	2021-2-25T00:25:39	2021-2-25T10:30:39	33; 33; 24	1.26 ± 0.06; 1.49 ± 0.07; 7.34 ± 0.18
XMM-Newton	0890700101	2021-8-2T17:10:55	2021-8-3T01:19:15	24; 24; 17	1.80 ± 0.09; 1.51 ± 0.08; 9.97 ± 0.25
NuSTAR	60702044002	2021-8-2T16:21:09	2021-8-3T09:31:09	31	12.76 ± 0.22; 11.78 ± 0.22
XMM-Newton	0890700201	2022-1-21T05:11:06	2022-1-21T14:06:32	32; 32; 26	2.39 ± 0.09; 2.52 ± 0.09; 11.64 ± 0.22
NuSTAR	60702044004	2022-1-21T06:46:09	2022-1-22T00:16:09	32	16.56 ± 0.24; 15.76 ± 0.23
XMM-Newton	0890700301	2022-2-4T10:20:38	2022-2-4T18:07:18	25; 25; 18	1.91 ± 0.09; 2.08 ± 0.09; 9.43 ± 0.23
NuSTAR	60702044006	2022-2-3T07:21:09	2022-2-3T21:31:09	28	16.72 ± 0.26; 16.24 ± 0.26

Note. All observations taken in 2021 and 2022 are analyzed here for the first time, while the 2017 observations were first studied by Zhao et al. (2019). The XMM-Newton count rates are computed in the 0.6–10 keV band, while the NuSTAR ones are computed in the 3–70 keV band. Exposures are computed after removing high-background periods.

Table 2
Summary of the Properties of the X-Ray Spectral Models Used in This Work

Model	Reference(s)	Material Distribution	Morphology	Free Parameters
MYTorus	Murphy & Yaqoob (2009) Yaqoob (2012) Yaqoob et al. (2015)	Uniform	Toroidal	Γ, $N_{\rm H,LOS}$ $N_{\rm H,tor}$, $A_{\rm S}$
borus02	Baloković et al. (2018)	Uniform	Sphere with biconical cutout	Γ, $N_{\rm H,LOS}$ θ_i, $N_{\rm H,tor}$, $f_{\rm c}$
UXCLUMPY	Buchner et al. (2019)	Clumpy	As proposed in Nenkova et al. (2008a)	Γ, $N_{\rm H,LOS}$ θ_i, TORσ, CTK

Note. MYTorus is used in its *decoupled* configuration (see the text for more details). Γ is the power-law photon index; $N_{\rm H,LOS}$ is the hydrogen column density between the observer and the accreting SMBH; $N_{\rm H,tor}$ is the (volume)-averaged column density of the obscuring material; $A_{\rm S}$ is the intensity of the reprocessed component with respect to the main one; θ_i is the angle between the torus axis and the observer; $f_{\rm c}$ is the obscuring material covering factor; TORσ is the angular width parameter, and models the vertical extent of the cloud population; finally, CTK is the covering factor of the inner obscuring ring. The free parameters reported in the table are those that were actually left free to vary in our analysis: further details are available in Saha et al. (2022).

3.2. Spectral Modeling

To avoid possible model-dependent effects, we analyze the NuSTAR and XMM-Newton spectra using three different physically motivated models that have been developed specifically to treat the X-ray spectra of heavily obscured AGN: we report a summary of their properties in Table 2. Two of these models assume that the obscuring material is uniformly distributed in a toroidal shape, while the third one works under the assumption that the obscuring material is distributed in clumps.

3.2.1. Uniform Torus Models

The first model we use in our analysis is MYTorus (Murphy & Yaqoob 2009; Yaqoob 2012; Yaqoob et al. 2015), which we use in its so-called *decoupled* configuration, where the LOS column density, $N_{\rm H,LOS}$, can in principle be different from the (volume) average column density, $N_{\rm H,tor}$. MYTorus works under the assumption that the obscuration in AGN is caused by a torus with a circular cross section, having a half-opening angle $\theta_{\rm T} = 60°$, where $\theta_{\rm T}$ is computed starting from the torus axis. This means that in MYTorus the torus covering factor is not a free parameter and is fixed to $f_c = \cos(\theta_{\rm T}) = 0.5$.

MYTorus is made of three separate components. In XSpec (Arnaud 1996) the model is written as follows:

$$C_{\rm NuS} * pha * (zpo1 * {\rm MYTZ} + A_{\rm S} * {\rm MYTS} + A_{\rm S} * {\rm MYTL} + f_{\rm S} * zpo2 + {\rm mekal}), \quad (1)$$

where *pha* is the absorption due to our own galaxy, $N_{\rm H,Gal} = 3.83 \times 10^{20}\,{\rm cm}^{-2}$ (Kalberla et al. 2005). The first MYTorus component, MYTZ, is an absorber applied to the direct continuum (modeled with a power law, *zpo*1) and is used to model the LOS absorption $N_{\rm H,LOS}$, the one caused by the material between the observer and the accreting SMBH. The second component, MYTS, models the so-called reprocessed (or scattered) emission, those photons that end up in the observer LOS after being up-scattered by the gas surrounding the AGN. Consequently, the column density of this component can be treated as a good approximation of the average torus column density, $N_{\rm H,tor}$. Finally, the third component, MYTL, models two typical fluorescence lines observed in AGN spectra, the iron Kα and Kβ lines at 6.4 and 7.06 keV, respectively. The relative intensity of the reprocessed component and the fluorescence lines with respect to the main power law is described by a constant, A_S. This constant takes into account the time delay between the main component intrinsic emission and the reprocessed one, which can therefore vary in intensity due to the well-known AGN variability. Furthermore, A_S can give some loose indication of the actual torus covering factor, since higher covering factors correspond to a larger intensity of the reprocessed component at energies >6 keV (see, e.g., Figure A1 in Zhao et al. 2020).

In MYTorus decoupled the inclination angle of the reprocessed component and the fluorescence lines can be fixed to one of two values: 90° or 0°. The 90° scenario is one where most of the reprocessed emission comes from material that is located between the accreting SMBH and the observer, while the 0° scenario is a *back-reflection* one, where most of the reprocessed emission is coming from the material located on the back side of the torus with respect to the observer perspective. In this paper, we test both configurations separately.

The second model we adopt for our analysis is borus02 (Baloković et al. 2018). borus02 works under the assumption that the shape of the obscuring material responsible for the reprocessed emission (including the iron Kα line) is a uniform-density sphere with two conical polar cutouts. The opening angle of these cutouts is a free parameter of the model.

In XSpec the model is written as follows:

$$C_{\rm NuS} * pha * ({\rm borus02} + zphabs * cabs * zpo1 + f_{\rm S} * zpo2 + {\rm mekal}). \quad (2)$$

The torus covering factor varies in the range $f_c = [0.1–1]$ (i.e., in a range of opening angles $\theta_{\rm T} = [0–84]°$). borus02 also includes as a free parameter the torus inclination angle $\theta_{\rm i}$, which is the angle between the observer and the torus axis. The LOS column density is modeled using the *zphabs* and *cabs* components.

Finally, as shown in Equations (1) and (2), our modeling includes three further components for both the MYTorus and the borus02 analysis. The first one is a cross-normalization constant between the XMM-Newton and the NuSTAR observations, $C_{\rm NuS}$, to model possible calibration offsets between the two instruments. Indeed, in all observations and with all models we find a cross normalization $C_{\rm NuS} \sim 1.1–1.15$, in agreement with previous results reported in the literature

(e.g., Madsen et al. 2017; Osorio-Clavijo et al. 2020; Baloković et al. 2021). In principle, there can be variability even between different cameras on the same instrument (MOS versus pn in XMM-Newton; FPMA versus FPMB in NuSTAR). However, we find that no additional cross-instrument components are required in our analysis, since when included in our fit they are always consistent with 1.

The second component is a secondary power law, *zpo*2, that treats the fraction of emission which is not affected by obscuration: this fractional value is parameterized with the constant f_s. Finally, NGC 1358 presents diffuse X-ray emission below 1 keV, which we model with a phenomenological thermal component `mekal`, where both the gas temperature and metallicity are left free to vary.

3.2.2. Clumpy Torus Model

Buchner et al. (2019) presented `UXCLUMPY`,[15] an X-ray spectral model which assumes that the AGN obscuration is caused by a clumpy distribution of material. More in detail, in `UXCLUMPY` the obscuring material is axisymmetric, and the number N of clouds between the observer and the accreting SMBH is

$$N = N_0 \cdot \exp\left\{-\left(\frac{\beta}{\mathrm{TOR}\sigma}\right)^2\right\}, \quad (3)$$

where N_0 is the number of clouds on the equatorial plane, β is the inclination angle toward the torus pole, and TORσ is the obscuring material angular width, which models the torus scale height and is a free parameter in the model. The clouds' angular size distribution is exponential and centered at $\theta_{\mathrm{cloud}} = 1°$, and the size of a single cloud is $D = d_{\mathrm{BH-cl}}\sin(\theta_{\mathrm{cloud}})$, where $d_{\mathrm{BH-cl}}$ is the distance between the cloud and the SMBH (Nenkova et al. 2008a, 2008b). Notably, `UXCLUMPY` (and more in general models where the obscuring material is assumed to be clumpy) allows one to set up a varying $N_{\mathrm{H,LOS}}$ scenario while keeping the obscurer geometry self-consistent.

Finally, `UXCLUMPY` includes an inner ring of Compton-thick material, whose covering factor CTK is a free parameter in the model. This additional component mimics a *reflection mirror,* which is needed to model an excess of reprocessed emission observed in some low-z, heavily obscured AGNs (Buchner et al. 2019) and can be linked, for example, to a *warped disk* obscurer (Buchner et al. 2021). In `XSpec`, the model is written as follows:

$$C_{\mathrm{NuS}} * pha * (\mathrm{uxclumpy} + f_{\mathrm{S}} * \mathrm{uxclumpy\_omni}) + \mathrm{mekal}, \quad (4)$$

where `UXCLUMPY` models both the transmitted and the reflected component (including the fluorescent lines), while `uxclumpy_omni` models the so-called *warm mirror emission*, which is the emission scattered, rather than absorbed by the obscuring material. The parameters of `UXCLUMPY` and `uxclumpy_omni` are linked. C_{NuS}, *pha*, f_{S}, and `mekal` are the same components described in Section 3.2.1.

[15] Which can be downloaded at https://github.com/JohannesBuchner/xars/blob/master/doc/uxclumpy.rst.

3.3. Evolution with Time of the Torus Properties

For consistency with previous works, and to test how joint multi-epoch spectral fitting can tighten the constraints on the spectral parameters, we performed a single-epoch spectral fit for each of the new observations reported in Table 1. We report a detailed description of these fits in the A4.

As discussed in Baloković et al. (2018, 2021), and more recently, in Saha et al. (2022), however, the simultaneous fit of multi-epoch X-ray spectra is the most efficient way to reduce the uncertainties on the different spectral parameters and break degeneracies between them. In particular, the multi-epoch fitting approach is key to put tight constraints on the torus covering factor, its average column density, and the inclination angle between the torus axis and the observer, three parameters that can be highly degenerate in single-epoch observations.

To further clarify the importance of multi-epoch observations, we report in Figure 3 four spectral parameters computed in each of the five single-epoch observations performed between 2017 August and 2022 February. We also note that the inclination angle θ_{i} between the observer and the torus axis is loosely constrained, if not fully unconstrained, in all single-epoch observations. Two of the parameters shown in the Figure are computed using `borus02`: the torus average column density (top left) and covering factor (top right). The other two are computed using `UXCLUMPY`: the obscuring material scale height (bottom left) and the covering factor of the inner reflector (bottom right).

The first clear evidence is that XMM-Newton observations alone are not effective in reliably constraining these parameters. More importantly, while both `UXCLUMPY` parameters are consistent, within the uncertainties, in each of the five epochs, both `borus02` parameters show evidence for variability. In particular, the variability in $N_{\mathrm{H,tor}}$ is found to be fairly large, varying in the range $\log N_{\mathrm{H,tor}} = [23.3–24.2]$. Such a disagreement between the single-epoch measurements should not be treated physically, given that the overall amount of material in the obscurer is not expected to vary in timescales of months. Rather, this result suggests that a uniform torus model is less efficient than a clumpy torus one in modeling the X-ray emission of NGC 1358, a result consistent with the idea that in this source the obscuring material surrounding the accreting SMBH is distributed in highly inhomogeneous clumps.

3.4. Joint Multi-epoch Fit

Given the limitations of a single-epoch fitting that we highlighted in the previous section, we performed a simultaneous fit of the NuSTAR and XMM-Newton spectra derived from the observations taken between 2017 August, and 2022 February, with the goal of reducing the parameters uncertainties and breaking cross-parameter degeneracies. We included in our models a cross-observation normalization to account for any flux variability not related to $N_{\mathrm{H,LOS}}$, and left the LOS column density free to vary in each of the six epochs: we assumed two independent $N_{\mathrm{H,LOS}}$ and normalization values for the NuSTAR and XMM-Newton observations taken on February 3 and 4. We then fit the spectra assuming no intra-epoch variability for all the other parameters: the power-law photon index Γ, the scattered fraction f_s, the average torus column density (in `MYTorus` and `borus02`), the torus covering factor (in `borus02` and `UXCLUMPY`).

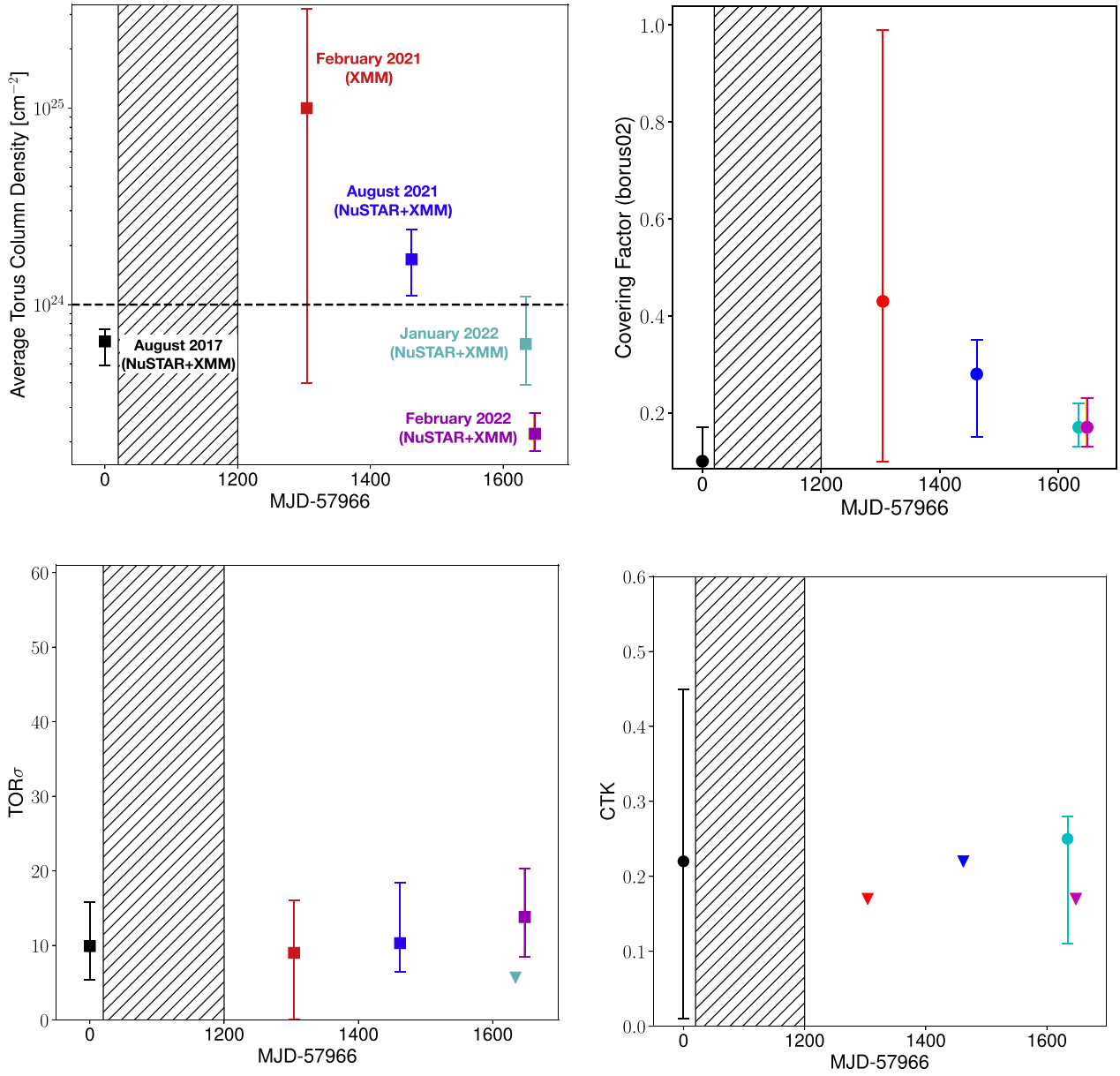

Figure 3. Different properties of the obscuring material derived from five single-epoch spectra (we report the results of the spectral analysis in the appendix. Top: torus average column density (left) and covering factor (right) as computed using `borus02`. Bottom: cloud vertical height, TORσ, and covering factor of the inner ring, CTK, as computed using `UXCLUMPY`. The color code is the same in all panels; to increase the plot clarity, the first 1200 days (hatched area) are not to scale. In the top left panel, the dashed horizontal line marks the $N_{\rm H,tor}$= 10^{24} cm^{-2} threshold. 90% confidence upper limits are plotted as downwards triangles.

We report in Table 3 the results of the multi-epoch fit, as well as the fractional variation of the uncertainties on the parameters with respect to the single-epoch results. The increase in count statistics and the use of multi-epoch data strongly reduce the uncertainties on all parameters. For example, the errors on the $N_{\rm H,LOS}$ values measured in the different epochs decrease by 10%–50% in `MYTorus` and `UXCLUMPY` and up to 80% in `borus02`. We also measure significant reductions in the uncertainties of the average torus column density (∼10%–50% in `MYTorus`; ∼80% in `borus02`) and in the torus covering factor (∼30%–50% in `UXCLUMPY`; ∼70% in `borus02`). Finally, the uncertainties on the power-law photon index decrease by 30%–70%. We note that the `borus02` best-fit photon index ($\Gamma = 1.45^{+0.01}_{-0.02}$) is close to the model's lower boundary ($\Gamma = 1.4$), another possible indirect evidence for the limitations of a uniform torus model to describe the NGC 1358 obscurer.

In Figure 4 we report the comparison between single-and multi-epoch 68%–90%–99% confidence contours of the torus covering factor and inclination angle as a function of the average torus column density, as measured using `borus02`, and of the torus vertical extent and inner ring covering factor, as measured with `UXCLUMPY`. For computational reasons, the multi-epoch contours have been computed using only the joint NuSTAR and XMM-Newton observations taken between 2021 August, and 2022 February (i.e., the 2021 February, and 2017 August observations are not included in the computation of the multi-epoch contours). For consistency, we thus compare these

Table 3
Summary of the Best-fit Results for the Joint Spectral Fit of All the NuSTAR and XMM-Newton Observations Taken between 2017 August 1 and 2022 February 3–4

	MYTorus Decoupled, 0°		MYTorus Decoupled, 90°		borus02		UXCLUMPY	
	Best Fit	% Err_{M-S}	Best Fit	% Err_{M-S}	Best Fit	% Err_{M-S}	Best Fit	% Err_{M-S}
χ^2/dof	2520.7/2457	...	2513.8/2457	...	2518.2/2457	...	2547.7/2457	...
Γ	$1.54^{+0.04}_{-0.04}$	50%	$1.54^{+0.04}_{-0.04}$	50%	$1.45^{+0.01}_{-0.02}$	75%	$1.58^{+0.03}_{-0.03}$	55%
$N_{H,LOS}$ 2017-8-1 [10^{24} cm^{-2}]	$1.68^{+0.15}_{-0.11}$	45%	$1.87^{+0.17}_{-0.15}$	60%	$1.64^{+0.05}_{-0.03}$	70%	$1.49^{+0.09}_{-0.10}$	60%
$N_{H,LOS}$ 2021-2-25 [10^{24} cm^{-2}]	$1.21^{+0.06}_{-0.05}$	60%	$1.26^{+0.07}_{-0.06}$	65%	$1.34^{+0.04}_{-0.03}$	60%	$1.02^{+0.08}_{-0.10}$	50%
$N_{H,LOS}$ 2021-8-2 [10^{24} cm^{-2}]	$0.87^{+0.04}_{-0.04}$	20%	$0.88^{+0.04}_{-0.04}$	50%	$0.87^{+0.02}_{-0.02}$	60%	$0.85^{+0.05}_{-0.06}$	30%
$N_{H,LOS}$ 2022-1-21 [10^{24} cm^{-2}]	$0.71^{+0.03}_{-0.03}$	30%	$0.71^{+0.03}_{-0.03}$	40%	$0.70^{+0.02}_{-0.01}$	60%	$0.70^{+0.03}_{-0.03}$	30%
$N_{H,LOS}$ 2022-2-3 [10^{24} cm^{-2}]	$0.74^{+0.04}_{-0.04}$	30%	$0.75^{+0.04}_{-0.04}$	40%	$0.73^{+0.02}_{-0.01}$	60%	$0.72^{+0.03}_{-0.03}$	25%
$N_{H,LOS}$ 2022-2-4 [10^{24} cm^{-2}]	$0.76^{+0.04}_{-0.04}$	40%	$0.77^{+0.04}_{-0.04}$	55%	$0.80^{+0.02}_{-0.03}$	55%	$0.74^{+0.04}_{-0.05}$	10%
$N_{H,tor}$ [10^{24} cm^{-2}]	$0.56^{+0.19}_{-0.11}$	80%	$0.36^{+0.05}_{-0.05}$	75%	$0.35^{+0.06}_{-0.03}$	85%	...	...
A_S	$0.21^{+0.03}_{-0.02}$	50%	$0.40^{+0.05}_{-0.05}$	85%	...	...	...	...
f_c	...	...	...	...	$0.17^{+0.02}_{-0.02}$	70%	...	...
θ_i [°]	...	...	...	...	87[f]	...	90[f]	...
TORσ [°]	...	...	...	...	...	...	$15.3^{+2.7}_{-2.5}$	60%
CTK	...	...	...	...	...	...	<0.10	30%
f_s 10^{-2}	$0.10^{+0.03}_{-0.03}$	55%	$0.16^{+0.03}_{-0.03}$	60%	$0.12^{+0.01}_{-0.02}$	75%	$0.28^{+0.10}_{-0.08}$	20%
kT (keV)	$0.63^{+0.03}_{-0.03}$	75%	$0.61^{+0.03}_{-0.03}$	70%	$0.65^{+0.03}_{-0.04}$	45%	$0.65^{+0.03}_{-0.03}$	70%
$Z/Z_\odot$	$0.05^{+0.02}_{-0.02}$	80%	$0.08^{+0.05}_{-0.03}$	95%	$0.05^{+0.01}_{-0.01}$	95%	$0.05^{+0.02}_{-0.02}$	60%
log(L_{2-10}) 2017-8-1 [erg s^{-1}]	$42.90^{+0.07}_{-0.10}$	...	$42.93^{+0.08}_{-0.09}$	...	$42.74^{+0.06}_{-0.09}$	...	$42.75^{+0.04}_{-0.04}$	...
log(L_{10-40}) 2017-8-1 [erg s^{-1}]	$43.74^{+0.23}_{-0.32}$	...	$43.38^{+0.24}_{-0.29}$	...	$43.11^{+0.33}_{-0.45}$	...	$42.93^{+0.13}_{-0.19}$	...
log(L_{2-10}) 2021-2-25 [erg s^{-1}]	$43.04^{+0.04}_{-0.05}$	...	$42.89^{+0.04}_{-0.04}$	...	$43.02^{+0.05}_{-0.05}$	...	$42.77^{+0.08}_{-0.10}$	...
log(L_{2-10}) 2021-8-2 [erg s^{-1}]	$42.96^{+0.04}_{-0.06}$	...	$42.96^{+0.04}_{-0.05}$	...	$42.93^{+0.05}_{-0.07}$	...	$42.91^{+0.04}_{-0.04}$	...
log(L_{10-40}) 2021-8-2 [erg s^{-1}]	$43.79^{+0.13}_{-0.21}$	...	$43.67^{+0.12}_{-0.21}$	...	$43.77^{+0.10}_{-0.15}$	...	$43.15^{+0.09}_{-0.13}$	...
log(L_{2-10}) 2022-1-21 [erg s^{-1}]	$42.99^{+0.07}_{-0.09}$	...	$42.98^{+0.04}_{-0.04}$	...	$42.91^{+0.04}_{-0.06}$	...	$42.95^{+0.03}_{-0.05}$	...
log(L_{10-40}) 2022-1-21 [erg s^{-1}]	$43.86^{+0.15}_{-0.32}$	...	$43.63^{+0.22}_{-0.28}$	...	$43.64^{+0.13}_{-0.26}$	...	$43.18^{+0.15}_{-0.20}$	...
log(L_{10-40}) 2022-2-3 [erg s^{-1}]	$43.55^{+0.16}_{-0.29}$	...	$43.45^{+0.17}_{-0.31}$	...	$43.53^{+0.14}_{-0.26}$	...	$43.21^{+0.14}_{-0.19}$	...
log(L_{2-10}) 2022-2-4 [erg s^{-1}]	$42.94^{+0.05}_{-0.06}$	...	$42.93^{+0.03}_{-0.04}$	...	$42.93^{+0.04}_{-0.06}$	...	$42.89^{+0.05}_{-0.06}$	...

Note. Γ is the main power-law component photon index. $N_{H,LOS}$ and $N_{H,tor}$ are the LOS and average column density, respectively, in units per cubic centimeter. A_S is the relative intensity of the reprocessed component with respect to the main one in MYTorus. f_c is the covering factor of the obscuring material as computed by borus02, $f_c = \cos(\theta_T)$, where θ_T is the angle (in degrees) between the axis of the torus and the edge of the torus. θ_i is the angle (in degrees) between the observer and the torus axis. In UXCLUMPY, TORσ is the angular width of the cloud population and CTK is the covering factor of the inner Compton-thick ring of clouds. kT and Z are the temperature (in keV) and metallicity (in units of solar metallicity) of the thermal mekal component. L_{2-10} and L_{10-40} are the intrinsic luminosities in units of ergs per second in the 2–10 and 10–40 keV bands, respectively. For all the parameters we report Err_{M-S}, the fractional change of the uncertainties with respect to the corresponding single-epoch observations (i.e., 30% means that the multi-epoch uncertainty on the parameter is 30% smaller than the average of the single-epoch uncertainties). The single-epoch results are reported in the A4.

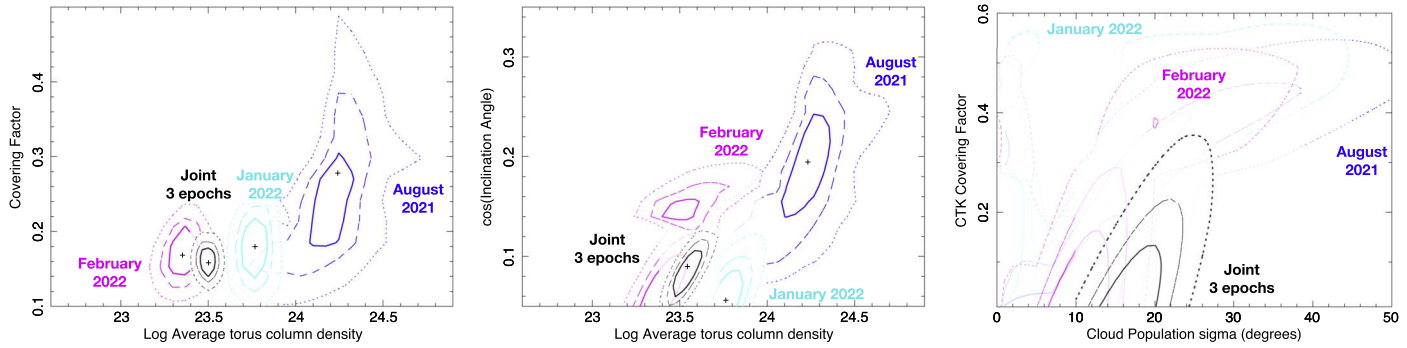

Figure 4. 68%, 90%, and 99% confidence contours of the covering factor as a function of the average torus column density (left), the cosine of the inclination angle as a function of the average torus column density (center), and the torus Compton-thick obscurer covering factor as a function of the cloud population opening angle, TORσ (right). The first two plots are obtained using borus02, and the third one using UXCLUMPY. The contours obtained from the multi-epoch joint fit are plotted in black, while those obtained fitting the various single-epoch spectra are color coded as in Figure 7.

multi-epoch contours with the single-epoch ones obtained in the three sets of observations.

For all three pairs of parameters, the multi-epoch fit allows one to break infra-parameter degeneracies and reliably confirm the *low-covering factor, Compton-thin average torus column density* scenario. Furthermore, the left and central plots once again highlight how single-epoch observations with borus02 can produce inconsistent $N_{H,tor}$ measurements, as we discussed

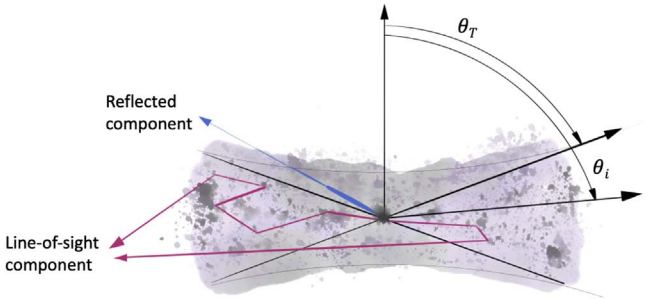

Figure 5. Sketch of the obscuring material surrounding NGC 1358, based on the best-fit results obtained in this work. θ_T is the torus opening angle, while θ_i is the angle between the observer and the torus axis.

in the previous section. In the multi-epoch fit, instead, we measure with `borus02` a Compton-thin average column density, $\log N_{\rm H,tor} = 23.5 \pm 0.1$, and a covering factor $f_c = 0.17 \pm 0.02$; the inclination angle is consistent with an *edge-on view* scenario, being $\theta_i > 83°$. We measure the same average torus column density using `MYTorus` decoupled in its 90° configuration: when using the 0° configuration, we measure a slightly larger average column density, but the uncertainties are also significantly larger ($\log N_{\rm H,tor} = 24.0^{+0.4}_{-0.7}$). Finally, with `UXCLUMPY` we measure a cloud vertical extent TOR$\sigma = 15.3^{+2.7}_{-2.5}°$ and an upper limit on the covering factor of the inner Compton-thick ring CTK < 0.10, once again confirming the low-f_c scenario. We report in Figure 5 a sketch of the NGC 1358 obscuring torus, based on these best-fit results.

4. Characterizing the Obscuring Material in NGC 1358

We report in Figure 6 the joint NuSTAR and XMM-Newton spectra of NGC 1358 taken in 2017 August, 2021 August, and 2022 January. The 2017 August spectrum is significantly fainter than the other two over the 2–60 keV range. A minor, but still notable difference is also observed between the 2021 August and the 2022 January observation, the second being brighter. To better quantify this variability between observations, and break the $N_{\rm H,LOS}$–luminosity degeneracy, we report in Figure 7 the evolution with time of two main parameters: the LOS column density (left) and the AGN 2–10 keV intrinsic, absorption-corrected luminosity (right). The best-fit values and uncertainties are those obtained jointly fitting the observations.

As it can be seen, the LOS column density of the material surrounding the accreting SMBH in NGC 1358 is highly variable over different timescales. The first and most significant change in $N_{\rm H,LOS}$ is the one observed between the 2017 observation and the 2021 February one. In a time span of ∼4 yr we observe a drop in $N_{\rm H,LOS}$ by ∼30% (from ~ 1.5–1.9×10^{24} to ~ 1.0–$1.3 \times 10^{23}\,{\rm cm}^{-2}$). We then observe a further ∼15%–30% reduction in a time span of about five months (from ~ 1.0–$1.3 \times 10^{23}\,{\rm cm}^{-2}$ on 2021 February 25, to 8–$9 \times 10^{23}\,{\rm cm}^{-2}$ on 2021 August 2), with a consequent transition from a Compton-thick to a Compton-thin state; a further ∼20% decrease, down to $7 \times 10^{23}\,{\rm cm}^{-2}$ is then observed between 2021 August and 2022 January. Finally, as shown in the inset of Figure 7, we measure a tentative, intriguing new increase in the two-week time span between our two most recent observations, although this last result is not confirmed by all models (in particular, this trend is stronger when fitting with `borus02`). Furthermore, we find some tentative evidence for ∼1 day variability thanks to the non-

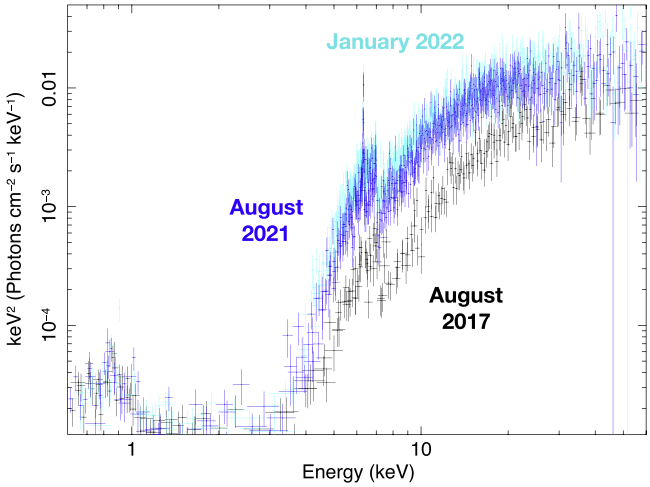

Figure 6. Unfolded spectra of the 2017 August (black), August 2021 (blue), and 2022 January (cyan) observations of NGC 1358, fitted using the `UXCLUMPY` model.

simultaneity of the NuSTAR and XMM-Newton 2022 February observations. We note that this evidence, while marginal, strengthens the *new* $N_{\rm H,LOS}$ *uprise* scenario (i.e., the $N_{\rm H,LOS}$ measured with XMM-Newton on 2022 February 4 is larger than the one measured with NuSTAR on 2022 February 3).

To better quantify the reliability of this $N_{\rm H,LOS}$ variability, one needs to check for potential degeneracies between parameters. In particular, it is essential to understand if the AGN intrinsic luminosity experienced any significant change in the time span covered by our X-ray observations. For this reason, we report in Figure 7, the evolution with time of the 2–10 keV luminosity as computed from our best-fit models. No significant trend with luminosity is detected, regardless of the model used to fit the data. We note that the 2–10 keV luminosity value for the 2017 observation decreased by a factor 2.5 with respect to the one reported in Zhao et al. (2019), and it is now consistent with the values measured in 2021–2022. Such a result suggests that single-epoch measurements are reliable when measuring parameters such as the LOS column density and (provided there is enough statistic above 10 keV) the torus average column density and covering factor. Single-epoch observations, however, are much less efficient in disentangling the contribution of the primary and reprocessed component to the overall emission, which consequently can lead to incorrect luminosity estimates.

To further underline that the high-quality NuSTAR and XMM-Newton data make it possible to break any $N_{\rm H,LOS}$–luminosity degeneracy, we show in Figure 8 the confidence contours of the LOS column density as a function of the cross-observation flux normalization.[16] This parameter takes into account any flux variability that is not related to $N_{\rm H,LOS}$ variability, and is therefore a good proxy of the 2–10 keV luminosity. As it can be seen, the $N_{\rm H,LOS}$ trend is still present and is therefore not significantly affected by AGN luminosity-related degeneracies.

[16] In all contours, the cross-observation normalizations are the XMM-Newton ones: the only exception being the February 3 contours, which are computed using the NuSTAR normalization for consistency with the fact that $N_{\rm H,LOS}$ is also measured from the NuSTAR data alone.

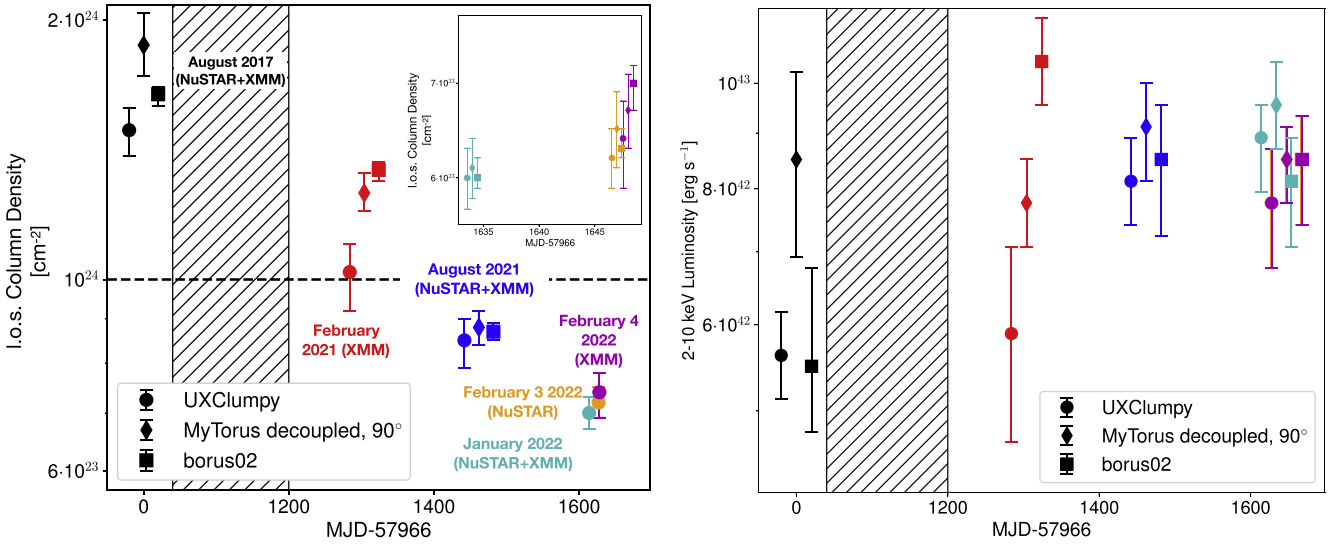

Figure 7. LOS column density (left) and 2–10 keV intrinsic luminosity (right) of NGC 1358 as obtained using UXCLUMPY (circles), MYTorus decoupled in its 90° configuration (diamonds) and borus02 (squares) in each of the epochs where an X-ray observation was performed, starting from the joint NuSTAR–XMM-Newton observation taken in 2017 August. No luminosity variability was observed between the 2022 February 3 and 4 observations, so we plot only one data point. In the left panel, we show in an inset the results of the 2022 observations, to avoid overcrowding the plot. The UXCLUMPY and borus02 data points are shifted by 20 days (0.5 days in the $N_{\rm H,LOS}$ inset) for visualization purposes. To further increase the plot clarity, the first 1200 days (hatched area) are not in scale.

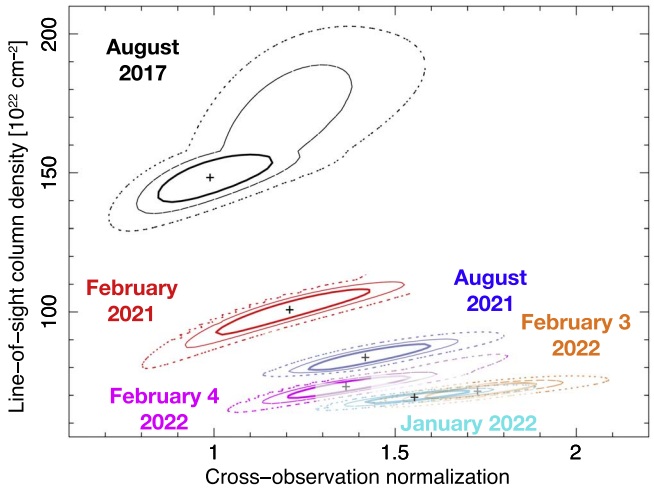

Figure 8. 68%, 90%, and 99% confidence contours of the LOS column density as measured using UXCLUMPY as a function of cross-observation flux normalization. In all contours, the cross-observation normalizations are the XMM-Newton ones: the only exception being the February 3 contours, which are computed using the NuSTAR normalization for consistency with the fact that $N_{\rm H,LOS}$ is also measured from the NuSTAR data alone. As discussed in the A4, the NuSTAR cross normalizations are usually ∼10% larger than the XMM-Newton ones.

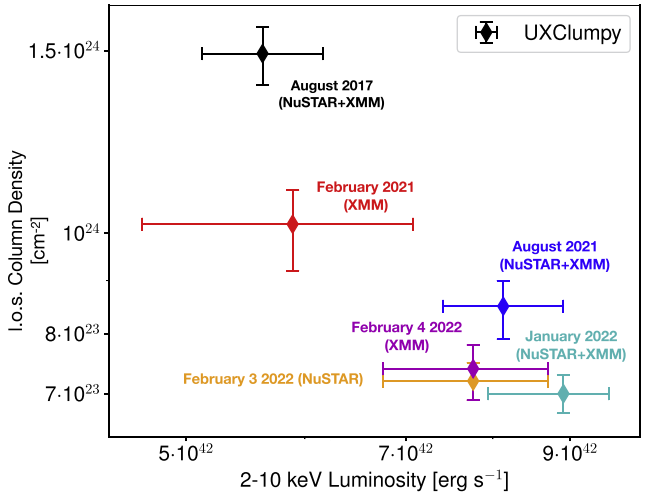

Figure 9. LOS column density as computed with UXCLUMPY as a function of the 2–10 keV intrinsic luminosity in NGC 1358. The color code for each observing epoch is the same used in Figures 3, 7, and 8.

In Figure 9, left panel, we plot the 2–10 keV luminosity as a function of $N_{\rm H,LOS}$, as computed using UXCLUMPY, to better underline the correlation between these two quantities.

A possible, qualitative explanation for the observed $N_{\rm H,LOS}$ and X-ray luminosity variability is a self-regulated *AGN feedback* scenario (see, e.g., Gaspari et al. 2020 for a review). We work under the assumption that the 2–10 keV luminosity can be used to estimate the AGN bolometric luminosity and can therefore be a proxy for the SMBH Eddington ratio, $\lambda_{\rm Edd} = L_{\rm bol}/L_{\rm Edd}$. We remark that there are several caveats to take into account with respect to this approach. In particular, there is observational evidence, particularly in Type I AGN, of a lack of correlation between variability in the X-ray continuum and variability in the bolometric luminosity. This suggests that

Table 4
Summary of the Cloud Properties Inferred from Each Pair of X-Ray Observations, Assuming That the $N_{\rm H,LOS}$ Variability Measured between Two Consecutive Epochs Is Due to a Single Cloud

Obs. Range YYYY/MM–YYYY/MM	t_{100} (100 ks)	$\Delta N_{\rm H,24}$ (10^{24} cm^{-2})	$d_{\rm BH,3RS}$ (pc)	$d_{\rm BH,15RS}$ (pc)
2017/8–2021/2	1126.7	0.61 ± 0.35	5.6×10^3	224
2021/2–2021/8	136.5	0.38 ± 0.15	82.2	3.3
2021/8–2022/1	148.6	0.17 ± 0.10	97.5	3.9
2022/1–2022/2	11.2	<0.14	0.56	0.02
2022/2–2022/2	0.9	<0.13	3.3×10^{-3}	1.3×10^{-4}

Note. $d_{\rm BH}$ is the distance between the cloud and the SMBH; t_{100} is the time difference between the two observations, in units of 100 ks; $\Delta N_{\rm H,24}$ is the difference in LOS hydrogen column density, in units of 10^{24} cm^{-2}. Finally, $d_{\rm BH,3RS}$ and $d_{\rm BH,15RS}$ are the cloud-SMBH distances computed assuming a coronal size equal to 3 and 15 $R_{\rm S}$, respectively.

Table 5
Summary of the Best-fit Results for the Spectral Fit of the Observations Taken on 2021 February 25 (XMM-Newton only) and on 2021 August 2 (NuSTAR and XMM-Newton)

Date	2021-2-25 (XMM-Newton Only)				2021-8-2 (NuSTAR + XMM-Newton)			
Model	MYTorus	MYTorus	borus02	UXCLUMPY	MYTorus	MYTorus	borus02	UXCLUMPY
	Decoupled, 0°	Decoupled, 90°			Decoupled, 0°	Decoupled, 90°		
χ^2/dof	132.1/150	136.6/150	130.3/149	123.7/148	660.5/599	662.0/599	659.9/598	658.1/598
$C_{\rm NuS}$	N/A	N/A	N/A	N/A	$1.13^{+0.07}_{-0.06}$	$1.12^{+0.07}_{-0.06}$	$1.13^{+0.07}_{-0.06}$	$1.11^{+0.07}_{-0.06}$
Γ	$1.90^{+0.29}_{-0.50*}$	$1.79^{+0.35}_{-0.39*}$	$1.75^{+0.47}_{-0.35*}$	$1.94^{+0.25}_{-0.39}$	$1.61^{+0.11}_{-0.10}$	$1.60^{+0.10}_{-0.10}$	$1.60^{+0.07}_{-0.09}$	$1.63^{+0.09}_{-0.07}$
norm 10^{-2}	$0.59^{+0.74}_{-0.46}$	$0.64^{+1.00}_{-0.49}$	$0.40^{+1.16}_{-0.28}$	$0.80^{+0.78}_{-0.49}$	$0.51^{+0.22}_{-0.13}$	$0.56^{+0.28}_{-0.19}$	$0.45^{+0.14}_{-0.10}$	$0.68^{+0.29}_{-0.18}$
$N_{\rm H,LOS}$ [10^{24} cm^{-2}]	$0.94^{+0.14}_{-0.20}$	$1.10^{+0.20}_{-0.20}$	$0.92^{+0.17}_{-0.10}$	$1.09^{+0.35}_{-0.05}$	$0.86^{+0.06}_{-0.05}$	$0.94^{+0.09}_{-0.09}$	$0.83^{+0.06}_{-0.05}$	$0.91^{+0.09}_{-0.08}$
$N_{\rm H,tor}$ [10^{24} cm^{-2}]	10.00^{+*}_{-*}	$0.28^{+0.10}_{-0.08}$	$10.05^{+21.57*}_{-9.62}$	...	$1.98^{+1.39}_{-1.50}$	$0.37^{+0.20}_{-0.10}$	$1.74^{+0.71}_{-0.59}$	...
A_S	$0.59^{+0.36}_{-0.21}$	$0.47^{+0.54}_{-0.19}$	...	...	$0.24^{+0.07}_{-0.08}$	$0.40^{+1.38}_{-0.11}$	...	...
f_c	...	...	$0.43^{+0.56}_{-0.33*}$	...	...	...	$0.28^{+0.07}_{-0.13}$	...
θ_i (°)	...	...	$67.3^{+17.2}_{-42.0}$	$65.9^{+17.0}_{-44.3}$	...	...	$78.7^{+4.2}_{-5.6}$	$87.8^{+2.2*}_{-9.8}$
TORσ (°)	...	...	...	$9.0^{+7.0}_{-8.9}$	...	...	...	$10.3^{+8.1}_{-3.9}$
CTK	...	...	...	<0.17	...	...	...	<0.22
f_s 10^{-2}	$0.15^{+0.46}_{-0.12}$	$0.21^{+0.34}_{-0.11}$	$0.19^{+0.47}_{-0.16}$	<0.28	$0.13^{+0.06}_{-0.05}$	$0.16^{+0.15}_{-0.06}$	$0.15^{+0.10}_{-0.09}$	$0.12^{+0.07}_{-0.12*}$
kT (keV)	$0.64^{+0.09}_{-0.11}$	$0.63^{+0.08}_{-0.12}$	$0.68^{+0.11}_{-0.10}$	$0.74^{+0.08}_{-0.11}$	$0.59^{+0.06}_{-0.10}$	$0.58^{+0.06}_{-0.10}$	$0.60^{+0.06}_{-0.10}$	$0.62^{+0.07}_{-0.08}$
$Z/Z_\odot$	$0.05^{+0.13}_{-0.03}$	$0.08^{+3.31}_{-0.06}$	$0.04^{+0.06}_{-0.02}$	$0.02^{+0.05}_{-0.01}$	$0.18^{+0.32}_{-0.12}$	$0.44^{+1.93}_{-0.37}$	$0.14^{+1.18}_{-0.10}$	$0.08^{+0.10}_{-0.05}$
$\log(F_{2\text{-}10})$ (erg s^{-1} cm^{-2})	$-12.06^{+0.02}_{-0.74}$	$-12.05^{+0.01}_{-0.29}$	$-12.05^{+0.23}_{-0.36}$	$-12.05^{+0.01}_{-0.36}$	$-11.83^{+0.01}_{-0.10}$	$-11.83^{+0.01}_{-0.07}$	$-11.83^{+0.03}_{-0.08}$	$-11.83^{+0.04}_{-0.33}$
$\log(F_{10\text{-}40})$ (erg s^{-1} cm^{-2})	N/A	N/A	N/A	N/A	$-10.68^{+0.01}_{-0.08}$	$-10.68^{+0.01}_{-0.05}$	$-10.68^{+0.01}_{-0.10}$	$-10.68^{+0.03}_{-0.49}$
$\log(L_{2\text{-}10})$ (erg s^{-1})	$42.84^{+0.05}_{-0.05}$	$42.95^{+0.05}_{-0.05}$	$42.80^{+0.10}_{-0.11}$	$42.85^{+0.12}_{-0.25}$	$42.97^{+0.05}_{-0.05}$	$43.02^{+0.04}_{-0.05}$	$42.92^{+0.07}_{-0.09}$	$42.99^{+0.16}_{-0.13}$
$\log(L_{10\text{-}40})$ (erg s^{-1})	N/A	N/A	N/A	N/A	$43.17^{+0.04}_{-0.03}$	$43.22^{+0.04}_{-0.03}$	$43.10^{+0.06}_{-0.05}$	$43.16^{+0.16}_{-0.10}$

Note. $C_{\rm NuS}$ is the cross normalization between NuSTAR and XMM-Newton. Γ and norm are the main power-law component photon index and normalization at 1 keV in photons keV^{-1} cm^{-2} s^{-1}, respectively. $N_{\rm H,LOS}$ and $N_{\rm H,tor}$ are the LOS and average column density, respectively, in units per cubic centimeter. A_S is the relative intensity of the reprocessed component with respect to the main one in MYTorus. f_c is the covering factor of the obscuring material as computed by borus02, $f_c = \cos(\theta_T)$, where θ_T is the angle (in degrees) between the axis of the torus and the edge of the torus. θ_i is the angle (in degrees) between the observer and the torus axis. In UXCLUMPY, TORσ is the angular width of the cloud population and CTK is the covering factor of the inner Compton-thick ring of clouds. kT and Z are the temperature (in keV) and metallicity (in units of solar metallicity) of the thermal mekal component. $F_{2\text{-}10}$ and F_{10-40} are the observed fluxes in units of erg per cubic centimeter per second at 2–10 and 10–40 keV, respectively. $L_{2\text{-}10}$ and L_{10-40} are the intrinsic luminosities in units of erg per second at 2–10 and 10–40 keV, respectively. Upper and lower limits flagged with * have reached the parameter boundary.

the observed X-ray luminosity variability might be linked to changes in the X-ray corona, particularly on short timescales like those sampled here.

We use Equation (21) from Marconi et al. (2004) to convert the 2–10 keV luminosities into bolometric luminosities. We then adopt the correlation between SMBH mass and stellar velocity dispersion reported in Gaspari et al. (2019) to compute the NGC 1358 SMBH mass, using the stellar velocity dispersion measured by Nelson & Whittle (1995), $\sigma_* = 173 \pm 14$ km s^{-1}. The SMBH mass is therefore $\log(M_{\rm BH}/M_\odot) = 8.22 \pm 0.15$: this value is slightly larger than the one reported by Woo & Urry (2002) using the Tremaine et al. (2002) correlation ($\log(M_{\rm BH}/M_\odot) = 7.88$). Based on these values, we find that the Eddington ratio might have only marginally varied from $\sim 4 \times 10^{-3}$ in 2017 to $\sim 5 \times 10^{-3}$ in 2021–2022. We note that the uncertainties on the Eddington ratio measurements can be fairly large, given that the intrinsic scatter in the $M_{\rm BH}$–σ_* we used is $\epsilon = 0.36 \pm 0.02$ (Gaspari et al. 2019). Indeed, when using the $M_{\rm BH}$–M_* relation from Suh et al. (2020), where M_* is computed from $\sigma_* = 173 \pm 14$ km s^{-1} using the Zahid et al. (2016) relation, we obtain $\log(M_{\rm BH}/M_\odot) = 7.51 \pm 0.75$. In a scenario where $\log(M_{\rm BH}/M_\odot) = 7.51$, the Eddington ratio of NGC 1358 would have been $\sim 2(4) \times 10^{-2}$ in 2017 (2021–2022).

Keeping in mind the above caveats, it is still helpful for the interested reader to discuss at least a qualitative physical interpretation of the retrieved obscuration, in particular in the currently accepted framework of self-regulated AGN feeding/feedback (e.g., Gaspari et al. 2020 for a review). Indeed, the AGN loop experiences a flickering alternation of feeding and feedback events on micro and macroscales over the several gigayear evolution. Specifically, higher obscuration phases are associated with stronger CCA rain (e.g., Gaspari et al. 2013, 2017), in which the feeding-dominated stage is driven by condensing cool clouds that rain down toward the meso—and ultimately the microscale, thus inducing higher $N_{\rm H,LOS}$ and lower luminosity (during 2017, as can be seen in Figure 9). Given the AGN self-regulation, such a process is expected to quickly trigger a feedback event (with higher AGN luminosities and lower $N_{\rm H,LOS}$) as soon as CCA has driven a critical mass inflow near the SMBH horizon. Given the uncertainties associated with our measurements, a definitive answer will be achieved by extending the X-ray monitoring campaign.

4.1. Modeling of the Obscuring Clouds Geometry through LOS Column Density Variability

Following Risaliti et al. (2002, 2005), the distance between the obscuring clouds and the SMBH can be computed with the equation

$$d_{\rm BH} = 600\, t_{100}^2\, n_{10}^2\, N_{\rm H,24}^{-2}\, R_{\rm S}, \quad (5)$$

where t_{100} is the variability time in units of 100 ks, n_{10} is the cloud density in units of 10^{10} cm^{-3} and $N_{\rm H,24}$ is the column density of a cloud in units of 10^{24} cm^{-2}. As mentioned above, based on the correlation between SMBH mass and stellar

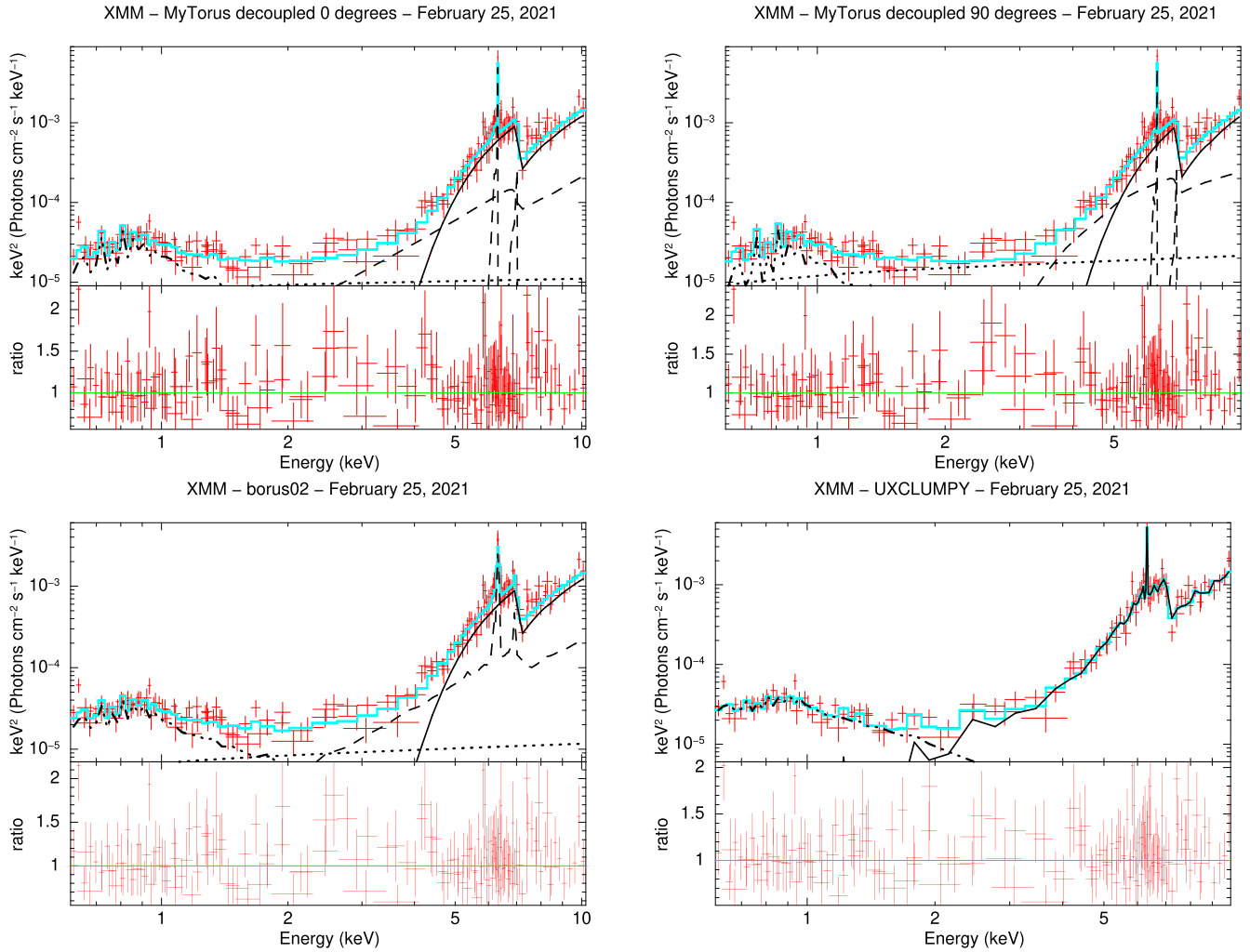

Figure 10. Unfolded XMM-Newton spectrum of the 2021 February 25 observation of NGC 1358. In the top panel we show the best fits obtained using `MYTorus` in its decoupled, $\theta = 0°$ (left) and $\theta = 90°$ configuration. In the bottom panel, we report the `borus02` (left) and `UXCLUMPY` (right) best-fit models. In all panels, the overall model is plotted as a solid cyan line, the absorbed main power-law component is plotted as a solid black line, the reprocessed emission as a dashed black line, the scattered component as the dashed black line, and the thermal `mekal` component as a dashed–dotted black line.

velocity dispersion, we measured an SMBH mass $\log(M_{\rm BH}/M_{\odot}) = 8.22 \pm 0.15$, so the Schwarzschild radius is $R_{\rm S} = \frac{2GM_{\rm BH}}{c^2} = 4.9 \times 10^{13}$ cm. We then work under the assumption that the variability observed between two consecutive observations is due to a single cloud having column density $N_{\rm H,24} = |N_{\rm H,Obs2} - N_{\rm H,Obs1}|/10^{24}$ passing between the observer and the X-ray emitter corona. Finally, it has been shown using a variety of methods that the X-ray corona size varies in the range $D = 3$–$15\,R_{\rm S}$ (e.g., McHardy et al. 2005; Fabian et al. 2009, 2015; Chartas et al. 2016; Kamraj et al. 2018), so that the cloud density can be computed as $n = \frac{|N_{\rm H,Obs2} - N_{\rm H,Obs1}|}{D}$.

We report in Table 4 the range of SMBH-cloud distances we obtain using the $N_{\rm H,LOS}$ variability and time separation between observations for the five consecutive pairs of observations taken between 2017 August and 2022 February. For consistency with the *clumpy torus scenario* that is suggested by our data, we use the $N_{\rm H,LOS}$ values obtained using `UXCLUMPY`: the results do not however change significantly when using the `borus02` or `MYTorus` LOS column density measurements.

Sampling different time separations allows us to sample different SMBH-cloud distances and/or cloud sizes. For example, the tentative $N_{\rm H,LOS}$ variability observed between the NuSTAR 2022 February 3 observation and the XMM-Newton 2022 February 4 one, if real, would be caused by material located at only a few hundred gravitational radii from the SMBH. Notably, this is the scale of the accretion disk itself for an SMBH with $M_{\rm BH} \sim 10^8\,M_{\odot}$, as measured through reverberation mapping (e.g., Jha et al. 2022). Timescales of $\sim$15 days like the one between our 2022 January and February observations, instead, sample clouds that are located at distances typically associated with the broad line region and the obscuring torus, which is from $\sim$0.02 pc (for a coronal size $D = 15\,R_{\rm S}$) to $\sim$1 pc (assuming $D = 3\,R_{\rm S}$). This is the so-called mesoscale for self-regulated AGN feeding/feedback (Gaspari et al. 2020), which is the crucial transitional regime linking the tiny SMBH physics to the macro properties of the host halo. We also note that $\sim 10^{-2}$ pc is the scale of the dust sublimation radius (i.e., the lower limit on the dusty torus inner boundary) for an AGN with 2–10 keV luminosity $\sim 10^{43}$ erg s^{-1} (see, e.g., Netzer 2015). We note, however, that the best-fit results for these last three epochs are consistent with a no-variability scenario.

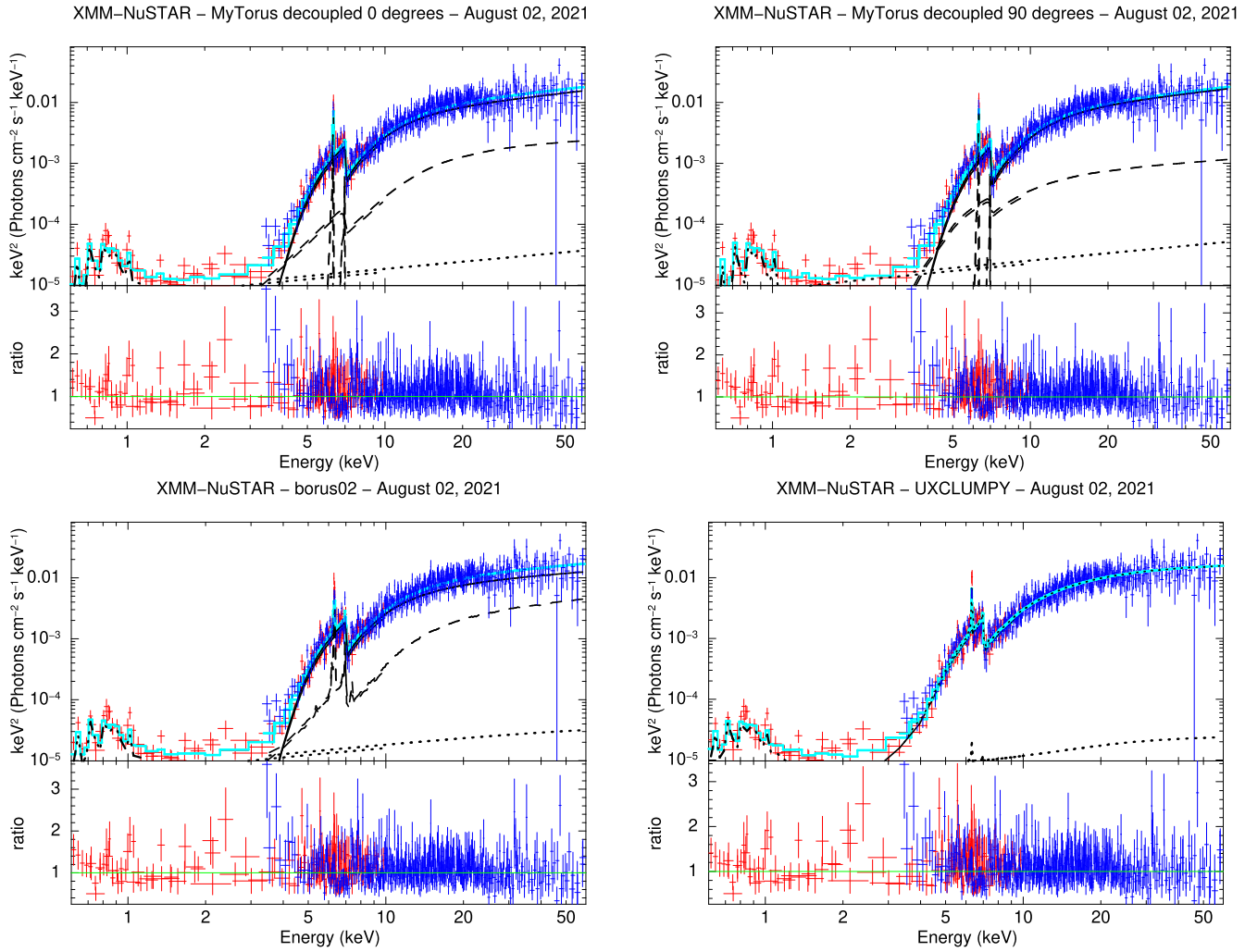

Figure 11. Unfolded XMM-Newton (red) and NuSTAR (blue) spectra of the 2021 August 2 observation of NGC 1358. In the top panel we show the best fits obtained using `MYTorus` in its decoupled, $\theta = 0^\circ$ (left) and $\theta = 90^\circ$ configuration. In the bottom panel, we report the `borus02` (left) and `UXCLUMPY` (right) best-fit models. In all panels, the overall model is plotted as a solid cyan line, the absorbed main power-law component is plotted as a solid black line, the reprocessed emission as a dashed black line, the scattered component as a dashed black line, and the thermal `mekal` component as a dashed–dotted black line.

Finally, observations taken a few months apart (such as our 2021 February and 2021 August ones, pair 2, or the latter and the 2022 January one, pair 3) probe distances of $\sim$1–10^2 pc, once again the looser constraint being associated with the more compact coronal size. We also note that the 4 yr time separation between the 2017 Compton-thick observation and the 2021 August one prevents us from reliably locating the material responsible for the high obscuration reported in Zhao et al. (2019), or even determining if this high-obscuration status was due to a single cloud or to a combination of clouds randomly interjecting our LOS.

5. Conclusions

In this paper, we presented the multi-epoch, NuSTAR and XMM-Newton 0.6–70 keV monitoring campaign of NGC 1358 which took place between 2021 February and 2022 February. The LOS column density of the target was predicted to be highly variable based on the properties of the obscuring material: namely, a small covering factor and a large offset between the Compton-thick LOS column density measured in 2017 August and the Compton-thin average torus column density. This evidence made the source an ideal candidate changing-look CT-AGN. We summarize the main results of this work.

1. The selection method we proposed to select candidate changing-look CT-AGNs turned out to be highly effective. We find that in 2021–2022 the LOS column density of the material surrounding the AGN in NGC 1358 decreased by a factor $\sim$3 with respect to the 2017 observation, and the source transitioned from Compton-thick to Compton-thin. This result opens the way for a more extended NuSTAR–XMM-Newton campaign to target the rest of the candidate changing-look CT-AGNs population and further characterize the properties of the obscuring material surrounding accreting SMBHs.
2. We found NGC 1358 to be LOS column density-variable over a wide range of timescales: these results suggest that the obscuring material is distributed in clouds of different $N_{\rm H,LOS}$ located at distances from the accreting SMBH as small as a few hundreds of gravitational radii and as large as tens to hundreds of parsec (depending on the cloud sizes). In such a scenario, a clumpy torus model offers a more self-consistent explanation to the $N_{\rm H,LOS}$ variability than a uniform torus one.

Table 6
Summary of the Best-fit Results for the Spectral Fit of the Observations Taken on 2021 January 21 and 2022 February 3–4

Date	2022-1-21 (NuSTAR + XMM-Newton)				2022-2-4 (NuSTAR + XMM-Newton)			
Model	MYTorus Decoupled, 0°	MYTorus Decoupled, 90°	borus02	UXCLUMPY	MYTorus Decoupled, 0°	MYTorus Decoupled, 90°	borus02	UXCLUMPY
χ^2/dof	796.9/792	796.2/792	795.1/792	795.6/792	634.7/650	634.9/650	631.8/650	634.6/650
$C_{\rm NuS}$	$1.12^{+0.05}_{-0.05}$	$1.11^{+0.05}_{-0.05}$	$1.11^{+0.04}_{-0.03}$	$1.11^{+0.05}_{-0.05}$	$1.14^{+0.27}_{-0.22}$	$1.10^{+0.28}_{-0.25}$	$1.07^{+0.04}_{-0.23}$	$1.20^{+0.21}_{-0.17}$
Γ	$1.53^{+0.07}_{-0.09}$	$1.51^{+0.07}_{-0.06}$	$1.44^{+0.09}_{-0.04*}$	$1.59^{+0.08}_{-0.04}$	$1.50^{+0.08}_{-0.08}$	$1.51^{+0.08}_{-0.08}$	$1.43^{+0.08}_{-0.03*}$	$1.55^{+0.05}_{-0.08}$
norm10^{-2}	$0.46^{+0.11}_{-0.09}$	$0.40^{+0.12}_{-0.08}$	$0.34^{+0.02}_{-0.06}$	$0.64^{+0.15}_{-0.09}$	$0.42^{+0.14}_{-0.11}$	$0.44^{+0.17}_{-0.12}$	$0.36^{+0.01}_{-0.09}$	$0.46^{+0.09}_{-0.09}$
$N_{\rm H,LOS}$ J [10^{24} cm^{-2}]	$0.69^{+0.04}_{-0.04}$	$0.67^{+0.06}_{-0.04}$	$0.67^{+0.04}_{-0.04}$	$0.70^{+0.03}_{-0.03}$	...	...	...	...
$N_{\rm H,LOS}$ X [10^{24} cm^{-2}]	...	...	...	...	$0.79^{+0.08}_{-0.07}$	$0.83^{+0.09}_{-0.08}$	$0.81^{+0.04}_{-0.08}$	$0.73^{+0.04}_{-0.05}$
$N_{\rm H,LOS}$ N [10^{24} cm^{-2}]	...	...	...	...	$0.73^{+0.06}_{-0.06}$	$0.75^{+0.07}_{-0.07}$	$0.72^{+0.02}_{-0.05}$	$0.69^{+0.04}_{-0.03}$
$N_{\rm H,tor}$ [10^{24} cm^{-2}]	$1.00^{+1.51}_{-0.52}$	$0.60^{+0.50}_{-0.28}$	$0.63^{+0.47}_{-0.24}$	...	$0.30^{+3.37}_{-0.12}$	$0.21^{+0.09}_{-0.06}$	$0.22^{+0.06}_{-0.04}$	...
A_S	$0.18^{+0.06}_{-0.05}$	$0.47^{+0.29}_{-0.16}$	...	...	$0.28^{+0.09}_{-0.09}$	$0.48^{+0.15}_{-0.13}$	...	...
f_c	...	...	$0.17^{+0.05}_{-0.04}$	...	...	...	$0.17^{+0.06}_{-0.04}$	...
θ_i (°)	...	...	87^f	90^f	...	...	87^f	90^f
TORσ (°)	...	...	...	<5.7	...	...	...	$13.8^{+6.5}_{-5.3}$
CTK	...	...	...	$0.25^{+0.03}_{-0.14}$	...	...	...	<0.17
f_s 10^{-2}	$0.10^{+0.05}_{-0.05}$	$0.18^{+0.05}_{-0.06}$	$0.19^{+0.03}_{-0.03}$	<0.14	<0.20	$0.10^{+0.10}_{-0.08}$	$0.12^{+0.11}_{-0.03}$	$0.19^{+0.12}_{-0.11}$
kT (keV)	$0.68^{+0.07}_{-0.06}$	$0.66^{+0.06}_{-0.06}$	$0.68^{+0.06}_{-0.05}$	$0.71^{+0.08}_{-0.06}$	$0.64^{+0.07}_{-0.14}$	$0.63^{+0.10}_{-0.15}$	$0.65^{+0.06}_{-0.05}$	$0.65^{+0.11}_{-0.12}$
$Z/Z_\odot$	$0.07^{+0.08}_{-0.03}$	$0.10^{+0.22}_{-0.06}$	$0.08^{+0.01}_{-0.01}$	$0.05^{+0.05}_{-0.02}$	$0.03^{+0.05}_{-0.02}$	$0.04^{+0.08}_{-0.03}$	$0.04^{+0.01}_{-0.04}$	$0.04^{+0.07}_{-0.03}$
$\log(F_{2\text{-}10})$ (erg s^{-1} cm^{-2})	$-11.66^{+0.01}_{-0.06}$	$-11.66^{+0.01}_{-0.09}$	$-11.66^{+0.05}_{-0.08}$	$-11.65^{+0.01}_{-0.03}$	$-11.75^{+0.01}_{-0.05}$	$-11.75^{+0.01}_{-0.04}$	$-11.75^{+0.06}_{-0.10}$	$-11.75^{+0.01}_{-0.03}$
$\log(F_{10\text{-}40})$ (erg s^{-1} cm^{-2})	$-10.60^{+0.02}_{-0.03}$	$-10.60^{+0.04}_{-0.06}$	$-10.60^{+0.07}_{-0.09}$	$-10.60^{+0.01}_{-0.02}$	$-10.61^{+0.01}_{-0.04}$	$-10.61^{+0.01}_{-0.04}$	$-10.61^{+0.09}_{-0.13}$	$-10.61^{+0.01}_{-0.03}$
$\log(L_{2\text{-}10})$ (erg s^{-1})	$42.98^{+0.06}_{-0.06}$	$42.93^{+0.04}_{-0.03}$	$42.92^{+0.06}_{-0.07}$	$42.98^{+0.10}_{-0.07}$	$42.94^{+0.08}_{-0.08}$	$42.97^{+0.09}_{-0.09}$	$42.95^{+0.10}_{-0.13}$	$42.88^{+0.09}_{-0.09}$
$\log(L_{10\text{-}40})$ (erg s^{-1})	$43.21^{+0.04}_{-0.04}$	$43.19^{+0.03}_{-0.03}$	$43.18^{+0.09}_{-0.12}$	$43.20^{+0.09}_{-0.07}$	$43.22^{+0.02}_{-0.02}$	$43.23^{+0.02}_{-0.02}$	$43.23^{+0.03}_{-0.04}$	$43.18^{+0.08}_{-0.09}$

Note. In the second data set, the XMM-Newton observation was performed on February 3 and the NuSTAR one on February 4 (see the text for more details). $N_{\rm H,LOS}$ J is computed assuming no variability between the NuSTAR and XMM-Newton observations, while $N_{\rm H,LOS}$ X and $N_{\rm H,LOS}$ N are computed separately from the XMM-Newton and NuSTAR data, respectively. The other parameters are the same as reported in Table 5. The inclination angle in borus02 and UXCLUMPY was frozen to the best-fit value because it was otherwise unconstrained if left free to vary. Upper and lower limits flagged with * have reached the parameter boundary.

3. Multi-epoch X-ray observations with NuSTAR and XMM-Newton are, as of today, one of the most efficient methods to reliably measure geometrical properties of the torus such as its covering factor and clumpiness (i.e., difference between average and LOS column density). The three epoch fits we performed led to a reduction in the fit parameters uncertainties, with respect to the single-epoch fits, which vary from 20%–80%.
4. The high spectral data quality of the NuSTAR and XMM-Newton observations enables simultaneous measurements of $N_{\rm H,LOS}$ and 2–10 keV intrinsic luminosity (and therefore derive an estimate of the SMBH Eddington ratio) in each of the epochs we analyzed.
5. The anticorrelation between column density and luminosity (Figure 9) can be understood in the framework of a self-regulated AGN feeding and feedback cycle driven via CCA raining clouds (e.g., Gaspari et al. 2020). However, only by continuing to monitor with NuSTAR and XMM-Newton with such a remarkable AGN, we will be able to better constrain the current variability/obscuration trends and probe the detailed self-regulation in NGC 1358.

We thank the referee for the useful suggestions that helped us in improving the paper. We thank Mauro Dadina for granting us access to the Sbuccia cluster to compute the multi-epoch confidence contours. This research has made use of the NuSTAR Data Analysis Software (NuSTARDAS) jointly developed by the ASI Space Science Data Center (SSDC, Italy) and the California Institute of Technology (Caltech, USA). SM acknowledges funding from the INAF "Progetti di Ricerca di Rilevante Interesse Nazionale" (PRIN), Bando 2019 (project: "Piercing through the clouds: a multiwavelength study of obscured accretion in nearby supermassive black holes"). M. G. acknowledges partial support by NASA Chandra GO9-20114X and HST GO-15890.020/023-A, and the Black-HoleWeather program. F.S. acknowledges funding from the INAF mainstream 2018 program "Gas-DustPedia: A definitive view of the ISM in the local universe". This work makes use of Matplotlib (Hunter 2007) and NumPy (Harris et al. 2020).

Appendix
Single-epoch Spectral Fits of the NuSTAR and XMM-Newton Observations Analyzed in This Work

In this appendix we report the results of the single-epoch spectral fits performed on the NuSTAR and XMM-Newton observations taken between 2021 February and 2022 February. We also report here the images of the best-fit models obtained using MYTorus, borus02, and UXCLUMPY for the four sets of observations analyzed in this paper.

A1. XMM-Newton Observation, 2021 February 25

The first observation we analyze is the only one without simultaneous NuSTAR data and was taken by XMM-Newton on 2021 February 25. We report the results of our analysis in Table 5 and the best-fit spectra obtained with MYTorus and borus02 in Figure 10. There is a general good agreement between the results obtained with MYTorus (either assuming $\theta_S = 90°$ or $\theta_S = 0°$), borus02 and UXCLUMPY. In particular, we measure a typical AGN photon index $\Gamma = 1.8$–1.9 (although with fairly large uncertainties, $\Delta\Gamma \sim 0.4$) and an

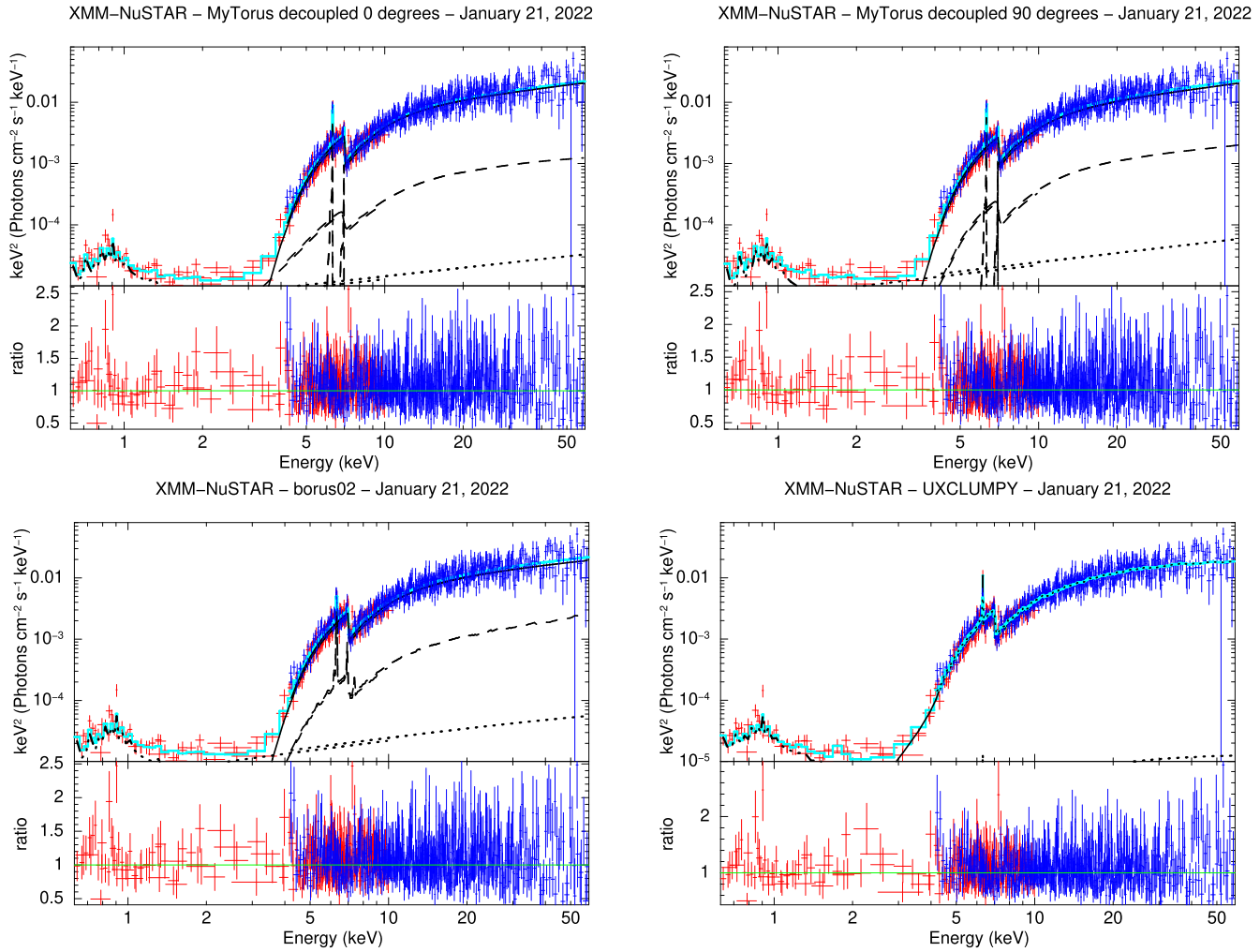

Figure 12. Unfolded XMM-Newton (red) and NuSTAR (blue) spectra of the 2022 January 21 observation of NGC 1358. In the top panel we show the best fits obtained using `MYTorus` in its decoupled, $\theta = 0°$ (left) and $\theta = 90°$ configuration. In the bottom panel, we report the `borus02` (left) and `UXCLUMPY` (right) best-fit models. In all panels, the overall model is plotted as a solid cyan line, the absorbed main power-law component is plotted as a solid black line, the reprocessed emission as a dashed black line, the scattered component as a dashed black line, and the thermal `mekal` component as a dashed–dotted black line.

LOS column density around the Compton-thick threshold, $N_{\rm H,LOS} \sim 10^{24}\,{\rm cm}^{-2}$.

The lack of NuSTAR data prevented us from constraining other parameters, such as the average column density and the covering factor, when fitting the data with `MYTorus` in one of its two configurations or with `borus02`. This is due to the fact that variations of $N_{\rm H,tor}$ or f_c mostly affect the >5–10 keV spectrum (see, e.g., Figure A1 in Zhao et al. 2020). The `UXCLUMPY` fit, which is also the one with the best reduced χ^2 ($\chi/{\rm dof} = 123.7/148$; as a reference, the `borus02` fit has $\chi/{\rm dof} = 130.3/149$), supports instead the *low-covering factor* scenario. Indeed, we measure a cloud vertical dispersion TOR$\sigma = 9.0^{+7.0}_{-8.9}°$ and a covering factor of the inner ring CTK < 0.17.

A2. NuSTAR and XMM-Newton Observations, 2021 August 2

The second observation analyzed in this work was taken quasi-simultaneously by NuSTAR and XMM-Newton on 2021 August 2. We report the results in Table 5, while the best-fit spectra are shown in Figure 11. There is a general excellent agreement between the results obtained with `MYTorus` (either assuming $\theta_S = 90°$ or $\theta_S = 0°$), `borus02` and `UXCLUMPY`, and all four models have almost identical reduced χ^2. We measure a typical AGN photon index $\Gamma \sim 1.6 \pm 0.1$ (slightly harder, although consistent within the uncertainties, than the one measured in the February 2021 observation) and an LOS column density just below the Compton-thick threshold, $N_{\rm H,LOS} \sim 8$–$9 \times 10^{23}\,{\rm cm}^{-2}$.

As for the other properties of the obscuring material, the average column density measured using `MYTorus` decoupled in its "0°" configuration is consistent with the one we measure with `borus02`, $\log N_{\rm H,tor} \sim 24.2$–$24.3$. Such a value is slightly larger than the one found by Zhao et al. (2019, $\log N_{\rm H,tor} \sim 23.8$), although the 2017 measurement is in agreement with the 2021 August one at the 90% confidence level. We also note that the $N_{\rm H,tor}$ obtained using `MYTorus` decoupled in its "90°" configuration is much lower ($\log N_{\rm H,tor} = 23.6 \pm 0.2$) and in even closer agreement with the Zhao et al. (2019) one. Finally, the covering factor we measure using `borus02` ($f_c = 0.28^{+0.08}_{-0.13}$) is in agreement with the one reported by Zhao et al. (2019, $f_c < 0.17$), and a similarly low-covering factor is found when using `UXCLUMPY` (TOR$\sigma = 10.3^{+8.1}_{-3.9}°$ and CTK < 0.22).

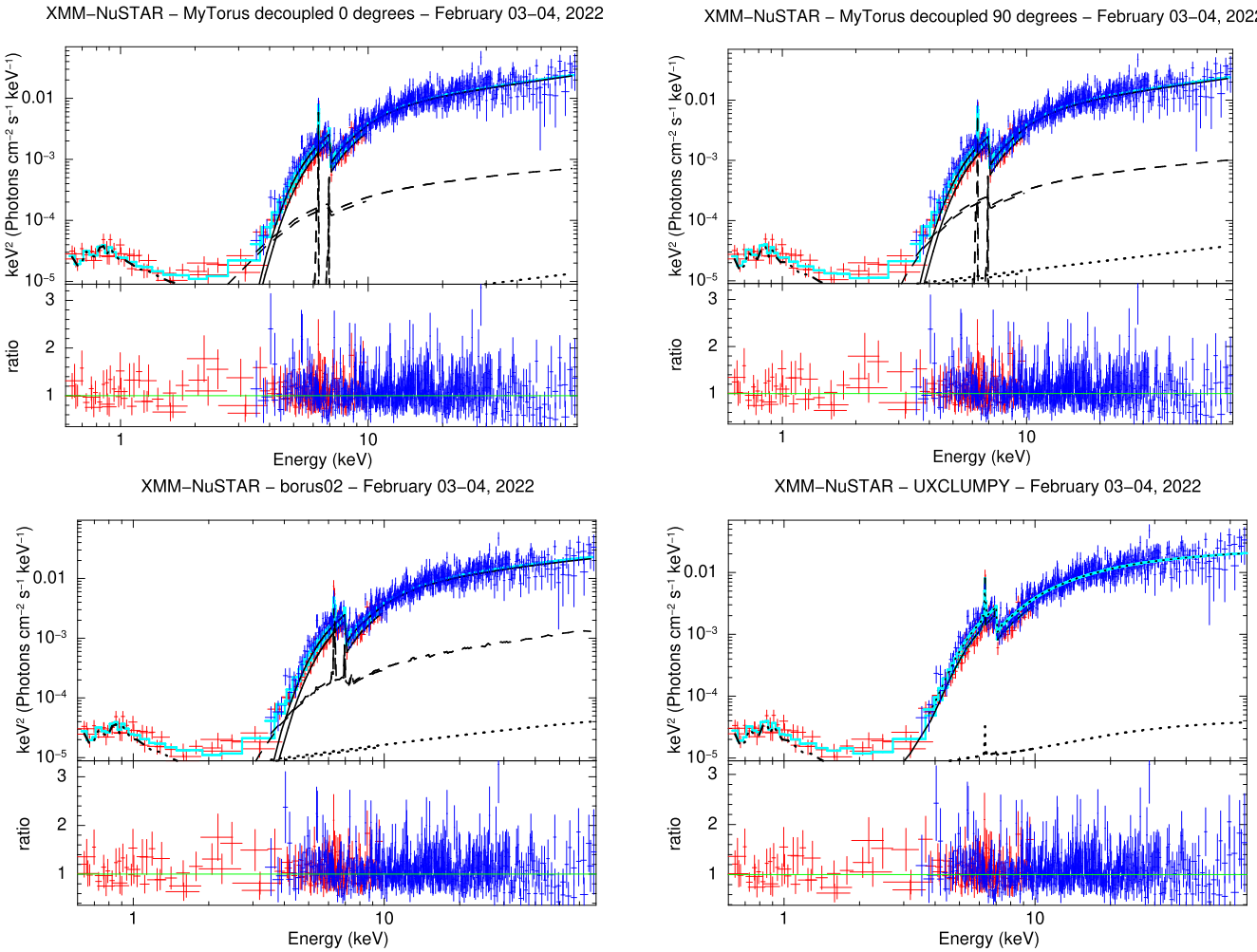

Figure 13. Unfolded XMM-Newton (red) and NuSTAR (blue) spectra of the 2022 February 3–4 observation of NGC 1358. On the top panel we show the best fits obtained using `MYTorus` in its decoupled, $\theta = 0°$ (left) and $\theta = 90°$ configuration. In the bottom panel, we report the `borus02` (left) and `UXCLUMPY` (right) best-fit models. In all panels, the overall model is plotted as a solid cyan line, the absorbed main power-law component is plotted as a solid black line, the reprocessed emission as a dashed black line, the scattered component as a dashed black line, and the thermal `mekal` component as a dashed–dotted black line.

A3. NuSTAR and XMM-Newton Observations, 2022 January 21

The third set of observations of NGC 1358 was performed quasi-simultaneously by NuSTAR and XMM-Newton on 2022 January 21. The results of the spectral analysis are reported in Table 6, while the spectra are shown in Figure 12. The LOS column density further decreased by ∼20% with respect to the observations performed 5.5 months earlier, being $\sim 7 \times 10^{23}\,\mathrm{cm}^{-2}$; such a result is model independent.

The agreement between the four models extends to all the other spectral parameters. In particular, both `borus02` ($f_c = 0.17^{+0.05}_{-0.04}$) and `UXCLUMPY` (TOR$\sigma < 5.7°$ and CTK $= 0.26^{+0.03}_{-0.14}$) once again favor a low-covering factor scenario, in agreement with our previous findings. The average torus column density is found to be $\log N_{\rm H,tor} \sim 23.8$ using both `borus02` and `MYTorus` decoupled in its 90° configuration. As mentioned before, such a value is the same reported in Zhao et al. (2019); furthermore, in this observation $N_{\rm H,LOS}$ is basically identical to $N_{\rm H,tor}$.

A4. NuSTAR and XMM-Newton Observations, 2022 February 3–4

The fourth and final set of NuSTAR and XMM-Newton observations was taken on 2022 February 3 and 4. We show the spectra and best-fit models in Figure 13. As reported in Table 1, the NuSTAR observation ended ∼13 hr before the start of the XMM-Newton observation. This small temporal offset allowed us to search for short-timescale variability. We first assumed that no $N_{\rm H,LOS}$ variability occurred between the two observations, and only allowed for flux variability which we parameterize with the usual cross-instrument constant $C_{\rm Nus}$. For all models, we find $C_{\rm Nus} = 1.31$–1.32 ± 0.07; as a comparison, in both the 2021 August and 2022 January observations we measure a cross normalization $C_{\rm Nus} \sim 1.1$. For this reason, we decided to leave $N_{\rm H,LOS}$ free to vary between the NuSTAR and XMM-Newton observations: with this new model, we obtain a cross normalization $C_{\rm Nus} \sim 1.1$, in close agreement with the values obtained in the other epochs. Furthermore, all models favor a scenario where $N_{\rm H,LOS}$ increased by 4–$9 \times 10^{22}\,\mathrm{cm}^{-2}$ between the February 3 NuSTAR observation and the XMM-Newton observation taken half a day later. We also note, however, that the two

$N_{\rm H,LOS}$ values are always in agreement within their 90% confidence uncertainties.

Regardless of the model we used to perform the spectral fit, the $N_{\rm H,LOS}$ variability scenario was always statistically favored with respect to the normalization-luminosity variability one; therefore, we report in Table 6 the results obtained with the double-$N_{\rm H,LOS}$ model. As mentioned above, there is tentative evidence for an increase in $N_{\rm H,LOS}$ within the two observations, and with respect to the January observation, particularly in the `MYTorus` and `borus02` models ($\Delta N_{\rm H,LOS} \sim 10^{23}\,{\rm cm}^{-2}$), while the discrepancy is milder when fitting the data with `UXCLUMPY`.

As for the average torus properties, all models support a low-f_c scenario with an average column density $N_{\rm H,tor} \sim 2\text{–}3 \times 10^{23}\,{\rm cm}^{-2}$.

ORCID iDs

S. Marchesi https://orcid.org/0000-0001-5544-0749
X. Zhao https://orcid.org/0000-0002-7791-3671
N. Torres-Albà https://orcid.org/0000-0003-3638-8943
M. Ajello https://orcid.org/0000-0002-6584-1703
M. Gaspari https://orcid.org/0000-0003-2754-9258
A. Pizzetti https://orcid.org/0000-0001-6412-2312
J. Buchner https://orcid.org/0000-0003-0426-6634
E. Bertola https://orcid.org/0000-0001-5487-2830
A. Comastri https://orcid.org/0000-0003-3451-9970
A. Feltre https://orcid.org/0000-0001-6865-2871
R. Gilli https://orcid.org/0000-0001-8121-6177
G. Lanzuisi https://orcid.org/0000-0001-9094-0984
G. Matzeu https://orcid.org/0000-0003-1994-5322
F. Pozzi https://orcid.org/0000-0002-7412-647X
F. Salvestrini https://orcid.org/0000-0003-4751-7421
R. Silver https://orcid.org/0000-0001-6564-0517
F. Tombesi https://orcid.org/0000-0002-6562-8654
A. Traina https://orcid.org/0000-0003-1006-924X
C. Vignali https://orcid.org/0000-0002-8853-9611
L. Zappacosta https://orcid.org/0000-0002-4205-6884

References

Arévalo, P., Bauer, F. E., Puccetti, S., et al. 2014, ApJ, 791, 81
Arnaud, K. A. 1996, in ASP Conf. Ser. 101, Astronomical Data Analysis Software and Systems V, ed. G. H. Jacoby & J. Barnes (San Francisco, CA: ASP), 17
Baloković, M., Brightman, M., Harrison, F. A., et al. 2018, ApJ, 854, 42
Baloković, M., Cabral, S. E., Brenneman, L., & Urry, C. M. 2021, ApJ, 916, 90
Baloković, M., Comastri, A., Harrison, F. A., et al. 2014, ApJ, 794, 111
Barthelmy, S. D., Barbier, L. M., Cummings, J. R., et al. 2005, SSRv, 120, 143
Bennett, C. L., Larson, D., Weiland, J. L., & Hinshaw, G. 2014, ApJ, 794, 135
Bianchi, S., Piconcelli, E., Chiaberge, M., et al. 2009, ApJ, 695, 781
Buchner, J., Brightman, M., Baloković, M., et al. 2021, A&A, 651, A58
Buchner, J., Brightman, M., Nandra, K., Nikutta, R., & Bauer, F. E. 2019, A&A, 629, A16
Burtscher, L., Meisenheimer, K., Tristram, K. R. W., et al. 2013, A&A, 558, A149
Chartas, G., Rhea, C., Kochanek, C., et al. 2016, AN, 337, 356
Elitzur, M., & Shlosman, I. 2006, ApJL, 648, L101
Fabian, A. C., Lohfink, A., Kara, E., et al. 2015, MNRAS, 451, 4375
Fabian, A. C., Zoghbi, A., Ross, R. R., et al. 2009, Natur, 459, 540
Feltre, A., Hatziminaoglou, E., Fritz, J., & Franceschini, A. 2012, MNRAS, 426, 120
Filippenko, A. V., & Sargent, W. L. W. 1985, ApJS, 57, 503
Gaspari, M., Eckert, D., Ettori, S., et al. 2019, ApJ, 884, 169
Gaspari, M., Ruszkowski, M., & Oh, S. P. 2013, MNRAS, 432, 3401
Gaspari, M., Temi, P., & Brighenti, F. 2017, MNRAS, 466, 677
Gaspari, M., Tombesi, F., & Cappi, M. 2020, NatAs, 4, 10
Gehrels, N., Chincarini, G., Giommi, P., et al. 2004, ApJ, 611, 1005
Gilli, R., Comastri, A., & Hasinger, G. 2007, A&A, 463, 79
Guainazzi, M., La Parola, V., Miniutti, G., Segreto, A., & Longinotti, A. L. 2012, A&A, 547, A31
Harris, C. R., Millman, K. J., van der Walt, S. J., et al. 2020, Natur, 585, 357
Hickox, R. C., & Alexander, D. M. 2018, ARA&A, 56, 625
Hönig, S. F., & Beckert, T. 2007, MNRAS, 380, 1172
Hunter, J. D. 2007, CSE, 9, 90
Jaffe, W., Meisenheimer, K., Röttgering, H. J. A., et al. 2004, Natur, 429, 47
Jansen, F., Lumb, D., Altieri, B., et al. 2001, A&A, 365, L1
Jha, V. K., Joshi, R., Chand, H., et al. 2022, MNRAS, 511, 3005
Jones, D. H., Read, M. A., Saunders, W., et al. 2009, MNRAS, 399, 683
Kalberla, P. M. W., Burton, W. B., Hartmann, D., et al. 2005, A&A, 440, 775
Kamraj, N., Harrison, F. A., Baloković, M., Lohfink, A., & Brightman, M. 2018, ApJ, 866, 124
Koss, M. J., Assef, R., Baloković, M., et al. 2016, ApJ, 825, 85
Koss, M. J., Romero-Cañizales, C., Baronchelli, L., et al. 2015, ApJ, 807, 149
Lawrence, A. 1991, MNRAS, 252, 586
Maccagni, F. M., Serra, P., Gaspari, M., et al. 2021, A&A, 656, A45
Madsen, K. K., Beardmore, A. P., Forster, K., et al. 2017, AJ, 153, 2
Marchese, E., Braito, V., Della Ceca, R., Caccianiga, A., & Severgnini, P. 2012, MNRAS, 421, 1803
Marchesi, S., Ajello, M., Comastri, A., et al. 2017, ApJ, 836, 116
Marchesi, S., Ajello, M., Marcotulli, L., et al. 2018, ApJ, 854, 49
Marchesi, S., Ajello, M., Zhao, X., et al. 2019, ApJ, 872, 8
Marconi, A., Risaliti, G., Gilli, R., et al. 2004, MNRAS, 351, 169
Marinucci, A., Bianchi, S., Nicastro, F., Matt, G., & Goulding, A. D. 2012, ApJ, 748, 130
Masini, A., Comastri, A., Baloković, M., et al. 2016, A&A, 589, A59
Mason, R. E., Rodríguez-Ardila, A., Martins, L., et al. 2015, ApJS, 217, 13
McHardy, I. M., Gunn, K. F., Uttley, P., & Goad, M. R. 2005, MNRAS, 359, 1469
McKinley, B., Tingay, S. J., Gaspari, M., et al. 2022, NatAs, 6, 109
Miniutti, G., Sanfrutos, M., Beuchert, T., et al. 2014, MNRAS, 437, 1776
Murphy, K. D., & Yaqoob, T. 2009, MNRAS, 397, 1549
Nelson, C. H., & Whittle, M. 1995, ApJS, 99, 67
Nenkova, M., Sirocky, M. M., Ivezić, Ž., & Elitzur, M. 2008a, ApJ, 685, 147
Nenkova, M., Sirocky, M. M., Nikutta, R., Ivezić, Ž., & Elitzur, M. 2008b, ApJ, 685, 160
Netzer, H. 2015, ARA&A, 53, 365
Oda, S., Tanimoto, A., Ueda, Y., et al. 2017, ApJ, 835, 179
Olivares, V., Salome, P., Hamer, S. L., et al. 2022, arXiv:2201.07838
Osorio-Clavijo, N., González-Martín, O., Papadakis, I. E., Masegosa, J., & Hernández-García, L. 2020, MNRAS, 491, 29
Puccetti, S., Comastri, A., Fiore, F., et al. 2014, ApJ, 793, 26
Ricci, C., Bauer, F. E., Treister, E., et al. 2016, ApJ, 819, 4
Ricci, C., Ueda, Y., Koss, M. J., et al. 2015, ApJL, 815, L13
Risaliti, G., Elvis, M., Fabbiano, G., et al. 2007, ApJL, 659, L111
Risaliti, G., Elvis, M., Fabbiano, G., Baldi, A., & Zezas, A. 2005, ApJL, 623, L93
Risaliti, G., Elvis, M., & Nicastro, F. 2002, ApJ, 571, 234
Rivers, E., Baloković, M., Arévalo, P., et al. 2015, ApJ, 815, 55
Rose, T., Edge, A. C., Combes, F., et al. 2019, MNRAS, 489, 349
Saha, T., Markowitz, A. G., & Buchner, J. 2022, MNRAS, 509, 5485
Simpson, C. 2005, MNRAS, 360, 565
Suh, H., Civano, F., Trakhtenbrot, B., et al. 2020, ApJ, 889, 32
Temi, P., Gaspari, M., Brighenti, F., et al. 2022, ApJ, 928, 150
Theureau, G., Bottinelli, L., Coudreau-Durand, N., et al. 1998, A&AS, 130, 333
Torres-Albà, N., Marchesi, S., Zhao, X., et al. 2021, ApJ, 922, 252
Traina, A., Marchesi, S., Vignali, C., et al. 2021, ApJ, 922, 159
Tremaine, S., Gebhardt, K., Bender, R., et al. 2002, ApJ, 574, 740
Woo, J.-H., & Urry, C. M. 2002, ApJ, 579, 530
Yaqoob, T. 2012, MNRAS, 423, 3360
Yaqoob, T., Tatum, M. M., Scholtes, A., Gottlieb, A., & Turner, T. J. 2015, MNRAS, 454, 973
Zahid, H. J., Geller, M. J., Fabricant, D. G., & Hwang, H. S. 2016, ApJ, 832, 203
Zaino, A., Bianchi, S., Marinucci, A., et al. 2020, MNRAS, 492, 3872
Zhao, X., Marchesi, S., Ajello, M., et al. 2019, ApJ, 870, 60
Zhao, X., Marchesi, S., Ajello, M., et al. 2021, A&A, 650, A57
Zhao, X., Marchesi, S., Ajello, M., Baloković, M., & Fischer, T. 2020, ApJ, 894, 71